Montanuniversität Leoben

An optimized biaxial stress temperature measurement for TiAlN based hard coatings

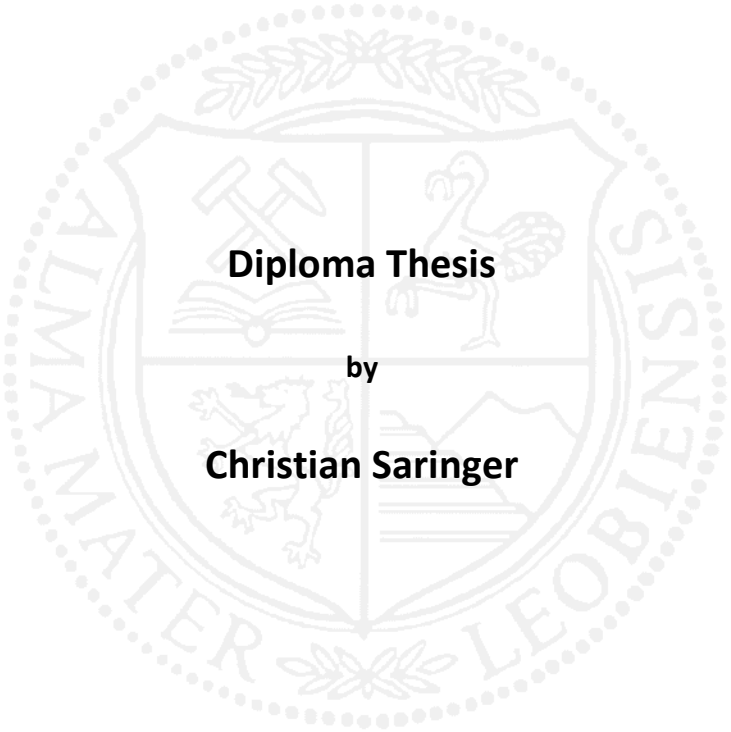

Diploma Thesis

by

Christian Saringer

This work has been carried out at the Chair of Functional Materials and Material Systems, Montanuniversität Leoben, Austria.

Leoben, March 2014

Financial support by the Austrian Federal Government (in particular from Bundesministerium für Verkehr, Innovation und Technologie and Bundesministerium für Wirtschaft, Familie und Jugend) represented by Österreichische Forschungsförderungsgesellschaft mbH and the Styrian and the Tyrolean Provincial Government, represented by Steirische Wirtschaftsförderungsgesellschaft mbH and Standortagentur Tirol, within the framework of the COMET Funding Programme is gratefully acknowledged.

Affidavit

I declare in lieu of oath, that I wrote this thesis and performed the associated research myself, using only literature cited in this volume.

Leoben, March 2014

Acknowledgments

My sincerest gratitude to Univ.-Prof. Dipl.-Ing. Dr. Christian Mitterer, head of the chair of functional materials and materials systems, for the professional supervision and efforts he put in me. *Thank you for giving me the opportunity to write my thesis on your chair!*

I am very grateful to my supervisor Dipl.-Ing. Michael Tkadletz, for his patience, friendship and the quick and exact corrections of this thesis. *Thank you for your skilled guidance as supervisor and climbing partner!*

I would like to express my gratitude to Ao.Univ.-Prof. Dipl.-Ing Dr. Reinhold Ebner, managing director of the Materials Center Leoben (MCL), for giving me the opportunity to carry out my thesis within an MCL project.

I would also like to thank Ing. Karl-Heinz Pichler and Felix Resch, for their help and assistance with the technical issues concerning the BSTM apparatus. *Thank you for helping me with the practical matters of my thesis!*

I am very thankful to Dipl.-Ing. Markus Pohler and Dipl.-Ing. Dr. Christoph Czettl from Ceratizit Austria, for providing the theme and the arc evaporated coatings for this thesis.

I am obliged to Priv.-Doz. Dr.techn. Beata Oswald-Tranta and Roland Schmidt from the chair of automation, for providing the nessecary knowledge and hardware for carrying out the infrared measurements.

Furthermore, I would like to thank the entire Thin Film Group, for the pleasant working atmosphere. Above all I owe thankfulness to Dipl.-Ing. Dr. Nina Schalk, for the additional advice for improving the quality of the present thesis. *Thanks to all of you for letting me be part of your group!*

I am deeply indebted to my Parents Elisabeth and Werner, for their encouragements and support since the very first day. *Thank you for providing me all opportunities that were necessary to achieve this degree!*

Finally, I want to express my appreciation to the love of my life Annemarie. *Thank you very much for the love and emotional support you have given to me since more than nine years!*

Table of Contents

Page

1 Introduction

Titanium aluminium nitride (TiAlN) has gained relevant importance as a coating material for mechanically loaded surfaces, where high wear resistance and good oxidational stability at elevated temperatures are of great importance [1-3]. Due to the high hardness and the formation of a protective aluminium oxide layer on the surface [4], lifetime during machining as well as cutting performance can be enhanced.

In order to deposit TiAlN, frequently used techniques are physical vapour deposition (PVD) processes such as cathodic arc evaporation [1-2] or magnetron sputtering [3]. Throughout these processes, deposition takes place under non-equilibrium conditions; thus residual stresses are typically created within the coating [5]. They influence the mechanical properties and thus the wear resistance to a great extent [6-8]. However, the residual stresses are not constant with temperature and stress relaxation at elevated temperatures might subsequently lead to a degradation of the mechanical properties [5,9]. Therefore, the investigation of the temperature dependence of the residual stresses is of huge interest. Quantifying the curvature of coated substrates using optical measurement techniques within a heated chamber has proven to be a simple way to determine the residual stresses as a function of temperature [10]. This procedure is commonly known as biaxial stress temperature measurement (BSTM), or wafer curvature method. In order to obtain precise results it is of vital importance to have a homogenous temperature distribution as well as reproducible conditions.

Therefore, the tasks treated within this work were the installation and calibration of a new heating device at an already existing BSTM apparatus and to examine the temperature behaviour of the residual stresses in TiAlN coatings deposited by the above mentioned processes. The chemical composition of the evaporated coatings has been varied as well as the bias voltage of the sputtered coatings. An extensive characterisation and comparison of the deposited films has been made in terms of mechanical properties, film thickness and thermal expansion. During investigation plastic deformation of the substrate at elevated temperatures occurred, which is described in this thesis as well.

2 Thin Film Fundamentals

2.1 Physical Vapour Deposition

Physical vapour deposition is a well-established process to deposit thin films with high hardness and high wear resistance [11,12]. Using such films, the lifetime and the efficiency of cutting tools can be significantly increased [13].

Every PVD-process consists of the following three essential steps [12]:

- Vapour formation of the film-forming species
- Transportation of the vapour from the target to the substrate
- Adsorption of the particles on the surface of the substrate, followed by nucleation and film growth

PVD can further be classified in the way how the target material is transformed into vapour phase [12]:

- Evaporation (by the use of e.g. a laser beam, electron beam or arc discharge)
- Sputtering (the atoms are transferred to the vapour phase by a momentum transfer of impinging positive gas ions)

A main advantage of PVD is its flexibility. The possibility of setting a huge variety of process parameters like pressure, distance between target and substrate, power density and bias voltage leads to a vast amount of potential coating materials [11]. Compared to chemical vapour deposition (CVD), the deposition temperature is rather low, which increases the number of possibly used substrate materials. Further, no potentially harmful process gases are needed [14]. Besides the use of compound targets, PVD offers the possibility to add reactive gases into the vacuum chamber in order to deposit chemical compounds, using metallic targets [13].

The coatings investigated within this work have been deposited by reactive magnetron sputtering and reactive cathodic arc evaporation. Thus, the following part shortly explains these two methods.

2.2 Sputtering

2.2.1 DC Sputtering

During sputter deposition the target atoms are evaporated by impinging ions. In order to create these, usually positively charged ions, a plasma is generated. By applying a negative voltage of about 1-5 kV [12], the ions are accelerated towards the target surface and transfer their kinetic energy when they hit the target [15]. With the intention of transforming atoms from the target into the gas phase, the transferred energy must be higher than their binding energy [16]. The sputtered atoms are mainly neutrals and travel on a ballistic path through the recipient and condense when they reach an obstacle. This can either be the substrate or the chamber walls, where subsequently a film is deposited [15,16]. The most commonly used working gas is argon, at typical pressures in the range of 10^{-2} mbar [15]. The basic setting of a sputter device is displayed in fig. 2.1. Substrate and target are positioned oppositely to each other within a vacuum chamber. The target acts as the cathode whilst the anode supports the substrate in this case. During deposition, the argon is induced through a flowmeter maintaining the required pressure.

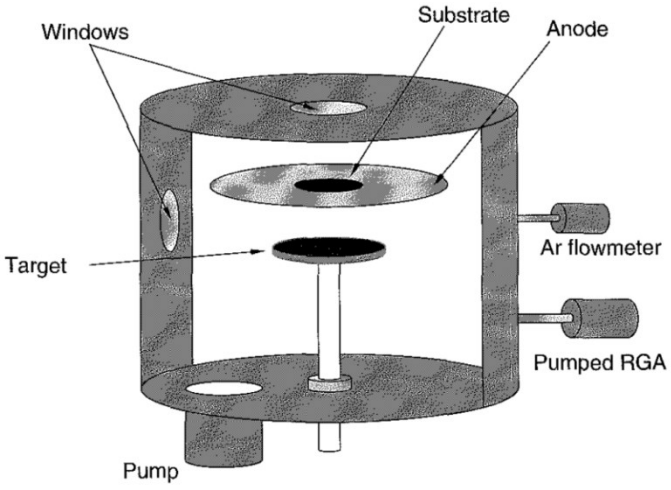

Fig. 2.1: Basic setting of a sputter device [17].

2.2.2 Pulsed DC Sputtering

As already mentioned above, a voltage is applied between target and chamber walls. The simplest possibility is a constant DC voltage. However, DC sputtering causes certain problems when depositing dielectric materials. They insulate the target from the plasma causing instabilities such as the formation of arcs by building up a charge and suddenly releasing it during deposition [18,19]. Furthermore, the target will block the DC current and no stable process can be maintained [19]. During bipolar pulsed DC sputtering, the target

potential is periodically switched from negative to positive. Any charging that occurs on the target during the negative pulse can dissipate during the positive pulse. Bipolar voltages can either be symmetric or asymmetric. Symmetric means, that the positive and negative amplitude are of the same value, whereas asymmetric determines an imbalance on the negative amplitude [18].

2.2.3 Bias Sputtering

Simple sputter deposition processes use substrate holders on mass potential. In contrast to that, during bias sputtering a comparatively low negative potential ranging from -50 to -500 V is applied to the substrate holder, leading to a negative substrate potential compared to the plasma [15]. This leads to an additional ion bombardment of the substrate surface and better film properties in general can be achieved [13,20,21]. The energy transfer of the impinging ions induces a higher mobility of the adsorbed atoms on the surface and therefore a denser film is produced [13]. The bias voltage has a big influence on the residual stresses of a coating as well [22], which is depicted in fig. 2.2. However, a removal of the film is simultaneously initiated by the ions, which causes a lower deposition rate though [20].

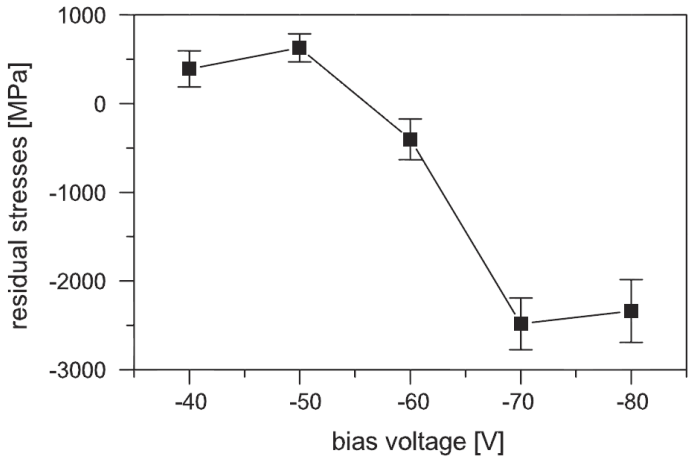

Fig. 2.2: Influence of the bias voltage on the residual stresses [23]. It can be seen that a higher bias voltage results in higher compressive residual stresses.

2.2.4 Magnetron Sputtering

By attaching an array of magnets behind the cathodes, and thus behind the targets, a magnetic field is superimposed over the electric field [17]. This magnetic field traps the electrons in front of the target and induces a movement perpendicular to the electric field lines. The density of electrons in the plasma near the target is significantly increased, causing a higher number of ionized argon atoms. Thus, in this region more atoms of the target are sputtered leading to a higher efficiency of the process [15,17,24]. Therefore, an erosion track

is formed, which is basically a zone of non-uniform wear (i.e. increased material removal). Its shape depends on the alignment of the magnets and limits the utilization of the target material [17]. A typically shaped erosion track is shown in fig. 2.3.

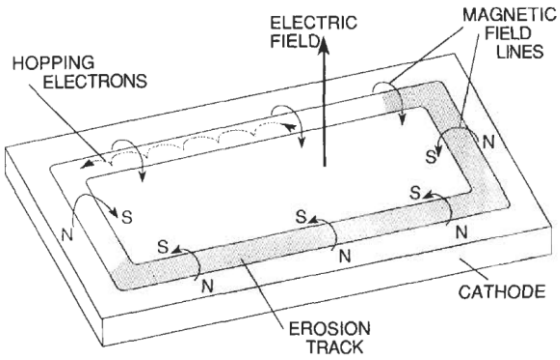

Fig. 2.3: Applied fields and electron movement during magnetron sputtering [24].

The magnetic field can either be balanced or unbalanced. Balanced magnetron sputtering means that the poles of the magnets are of the same strength. The magnetic field lines are thus closed and therefore loop over the target, see fig. 2.4a. Thus, the electrons are trapped solely in a small region near the target surface. During unbalanced magnetron sputtering, the strength of the poles is asymmetric, which causes the field lines to reach the substrate. Now, the electrons can follow the field lines to the surface of the substrate and ionize an additional number of atoms on their way. Consequently, the ion bombardment is increased on the substrate leading to dense, hard and adherent coatings [18]. Fig. 2.4b shows a typical setting of an unbalanced magnetron.

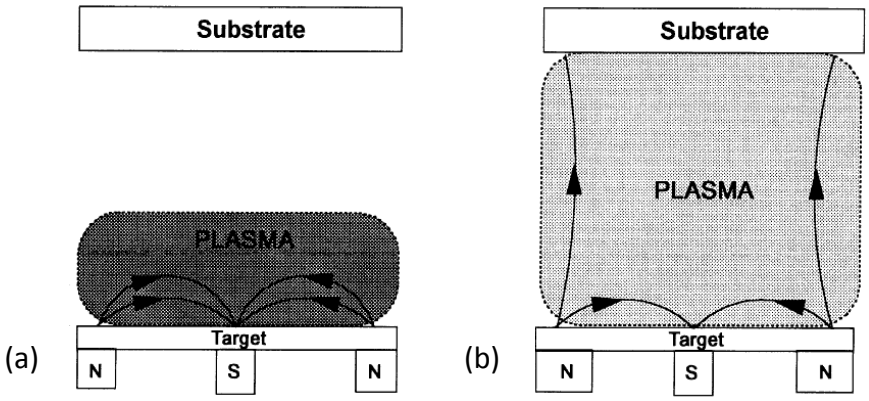

Fig. 2.4: Schematics of the magnetic field lines during (a) balanced and (b) unbalanced magnetron sputtering [25].

2.2.5 Reactive Sputtering

Reactive sputtering offers the possibility of depositing chemical compounds while metallic targets are used [18]. During this process, a reactive gas is added to the recipient which is chemically reacting with the atoms of the target material [13,15-18]. This reaction might either take place *(i)* on the target itself, i.e. the actual product is already sputtered, *(ii)* within the plasma or *(iii)* on the surface of the substrate. Usually the process gas is added as near as possible to the substrate in order to obtain *(iii)* [15]. Commonly used reactive gases are nitrogen, for the deposition of nitrides such as TiN, AlN [24] or TiAlN [3], or oxygen, in order to produce oxides such as Al_2O_3 or TiO_2 [15]. An important benefit of this process is the possibility of varying the stoichiometry by changing the partial pressure of the reactive gas [13]. However, during reactive magnetron sputtering the so called target poisoning can occur. When a certain partial pressure of the reactive gas is reached, an increased fraction of the target surface is covered by compounds [26]. If the compound is an electrical insulator, the quantity of sputtered material decreases rapidly, because the film builds up a charge which shields the target from the plasma [18].

2.3 Cathodic Arc Evaporation

Using cathodic arc evaporation, the target material is transferred into the gas phase by an electric discharge - called arc [27]. The deposition process can take place in high vacuum at an inert atmosphere or low pressure reactive gas. To ignite the arc, a grounded trigger must briefly contact the target surface, after which the procedure is self-sustaining. The arc is moving over the target surface in one or several cathode spots, which have a diameter of only a few microns and a lifetime of about 10^{-7} seconds [28]. Where the arcs hit the surface, usually at elevations, particles are ejected. A very dense local plasma is created obtaining extremely high current densities, which leads to an ionization of the ejected atoms of up to 90 % and more [27,28]. The particles are accelerated to a very large velocity by an explosive evaporation of surface asperities and hence reach an energy of about 20 - 200 eV, depending on the mass and ionization of the particles [29]. Due to the high particle energy it is possible to deposit dense and adherent coatings at substrate temperatures even below 200°C [12,28]. Compared to other PVD processes, the high ionisation rate offers the possibility of controlling the path and energy of the ions [29].

Fig. 2.5 shows the basic arrangement of the process consisting of the electrodes, a power supply, a control unit and the mechanical igniter, which works as the trigger. In order to improve the uniformity of material removal on the target, a magnetic coil can be attached behind the cathode controlling the movement of the arc. This variation is termed steered arc [12].

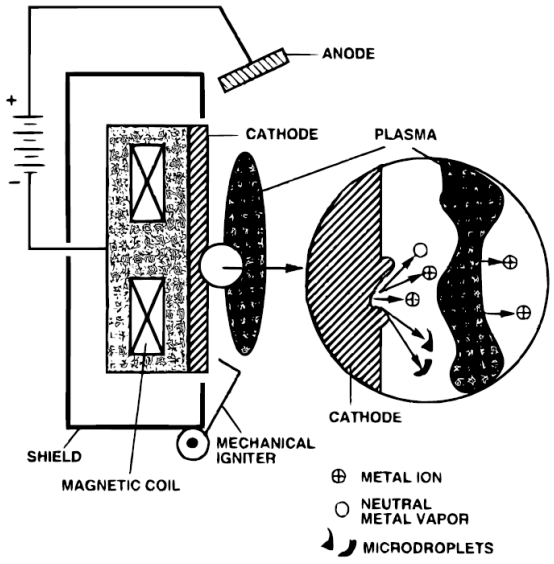

Fig. 2.5: Schematics of the arc evaporation process and detail of the cathode spot [24].

However, a drawback of arc evaporation is the formation of droplets [12,27-30]. Droplets are macroparticles, generated during evaporation, where the energy is not sufficient to sublimate the material, but only to melt it up [30]. Their average size is about 0.1 – 10 µm [29-31]. When these particles are incorporated in the coating, they cause local shadowing effects and thus voids during deposition. These voids act as diffusion paths, which have a negative effect on the oxidation behaviour [32]. Another effect is that macroparticle incorporation leads to an elevated surface roughness, which is of the order of the particle size [31].

2.4 Thin Film

2.4.1 Nucleation and Growth

Fig. 2.6 shows the basic particle interactions taking place on surfaces. Basically there are two ways how particles, condensing from the vapour state can interact. They might immediately be reflected, i.e. re-evaporated, or diffuse along the surface. Diffusing atoms can either be *(i)* adsorbed, particularly at special sites like edges on the surface or defects, or *(ii)* re-evaporate after a certain time. Besides the adsorption on edges and defects, several adsorbed particles can form clusters [33]. If their size is larger than a critical size, they will grow due to a reduction of energy and form nuclei; this is termed nucleation. Several of these growing nuclei compose a compact film when they coalescence [24]. Coalescence proceeds until a connected network is built up with unfilled channels in between. The channels are filled up as well with ongoing deposition until the film is thought to be continuous [24]. Substrate and film atoms might also interact by changing places, which is termed interdiffusion [33].

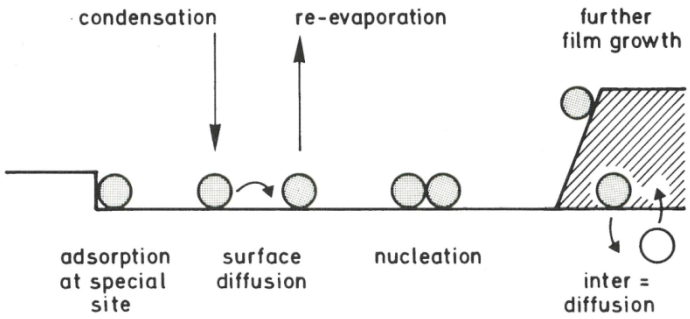

Fig. 2.6: Basic particle interactions on surfaces after condensing from the vapour state [33].

Three different types of film growth can be observed [24,33]. The first possibility is the so called layer by layer growth, which occurs if the interaction between substrate and layer atoms is stronger than within neighbouring layer atoms. A new layer only grows after the first one is completed, see fig. 2.7a. Contrary to that, the opposite case, i.e. where the interaction between the layer atoms is larger, leads to the so called island growth, where an island determines an agglomeration of atoms, see fig. 2.7c. The third case, i.e. layer plus island growth, is an intermediate situation, see fig 2.7b. After the formation of one to several complete monolayers, island growth can be detected. The lattice mismatch between film and substrate cannot be kept up into the bulk of the film. Therefore, the formation of monolayers is not possible anymore and island growth occurs [24,33].

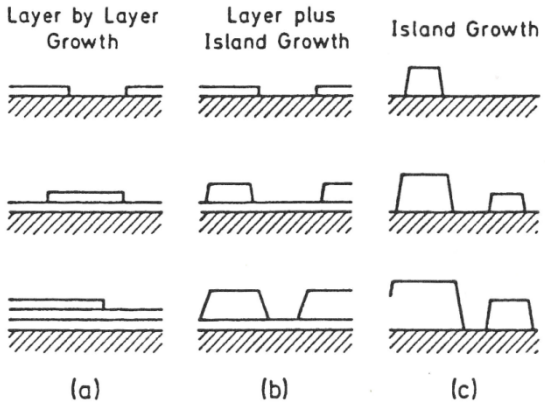

Fig. 2.7: Schematic representation of the three film growth modes: (a) layer by layer growth, (b) layer plus island growth and (c) island growth [33].

2.4.2 Microstructure

The microstructure and thus the properties of the film depend on various process parameters. The most important are substrate temperature, partial pressure and ion bombardment. A systematical analysis of the microstructure of PVD deposited films, with respect to the above mentioned parameters, led to the development of the so called structure zone model (SZM). This model qualitatively explains the microstructure development of the film as a function of adatom mobility, which is strongly determined by these process parameters [34].

Because the incident atoms have a preferred direction, the surface roughness of the substrate causes shadowing effects during deposition. These shadowing effects might be compensated by surface diffusion. The activation energy for diffusion of most pure metals is strongly depending on the melting temperature [12]. Thus, the microstructure of the growing film is determined by the ratio of substrate temperature and melting temperature T_s/T_m , termed the homologous temperature [12,35].

Movchan and Demchishin were the first to develop a model by investigating the structure of pure metals and oxides deposited by electron beam evaporation over the homologous temperature [36]. Thornton refined this model by adding another variable, i.e. the partial pressure of the inert gas, making the model applicable for sputtered films as well [37]. Applying a bias voltage provides the opportunity of influencing the crystal growth by inducing additional energy, as described in section 2.2.2. Therefore, studies with respect to bias voltage have been carried out by Messier *et* al., who further developed the Thornton model [38]. Fig. 2.8 shows the two zone models proposed by Thornton and Messier *et* al..

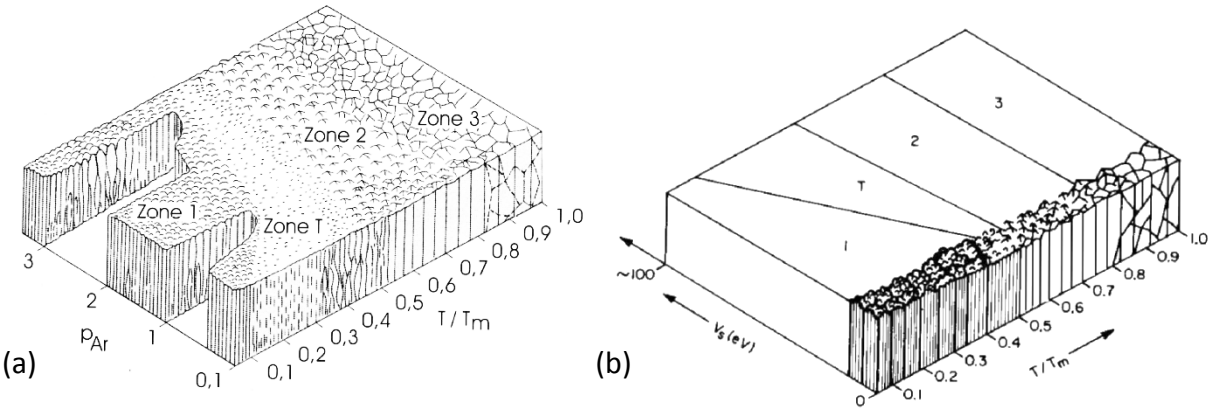

Fig. 2.8: Structure zone models proposed by (a) Thornton [12] and (b) Messier *et* al. [38], where p_A is the argon partial pressure and V_s is the bias voltage.

The basic model by Movchan and Demchishin is a three zone model. Zone one occurs at temperatures lower than 0.22 - 0.3 T_s/T_m and has a characteristic needle-structure. The diameter of the needles is increasing with higher temperature and coating thickness [12]. Neither bulk, nor surface diffusion are of importance, therefore the structure is porous and highly concentrated with defects [35]. Around 0.22 - 0.3 T_s/T_m, there is a smooth transition to zone two, which extends to a T_s/T_m ratio of about 0.45 - 0.5. The energy in this zone is approximately the activation energy for surface diffusion. The structure is clearly defined columnar, with increasing diameters of the columns at higher temperature [36,37]. Finally zone three, present at temperatures exceeding 0.5 T_s/T_m, has a structure of equiaxed grains and a bright surface due to the recrystallization that takes place within this zone [37].

Thornton introduced a transition zone between zone one and two. Its size is strongly depending on the argon pressure. At elevated pressures, adsorbed argon limits the mobility of adatoms which stabilises the porous structure of zone one leading to a smaller transition zone [37]. The structure of the transition zone is defined by the competitive growth of neighbouring crystals [35]. Messier *et* al. found that the bias voltage has a significant influence on the structure. The boundary between zone one and the transition zone is shifted to lower temperature with increasing bias voltage, while the boundary between zone two and transition zone is almost constant. The reason is the ion bombardment, which activates the mobility of the adatoms resulting in denser films [38]. The consequence is the possibility of producing denser films at lower temperature [13].

2.5 Coating Fundamentals

As a transition metal nitride, titanium nitride (TiN) has a bond structure that is a mixture of covalent, metallic and ionic fractions, which is responsible for the high hardness, wear resistance and chemical inertness [39]. TiN crystallizes in the face centred cubic (fcc) sodium chloride structure and forms a solid solution within a nitrogen concentration of about 37.5 - 50 at.% [39]. One of its major drawbacks, though, is the weak oxidation behaviour at temperatures above 500°C, which results in the formation of titanium dioxide, commonly known as rutile. This formation causes weak mechanical properties [4]. Adding aluminium as an alloying element to the system leads to the formation of a metastable, ternary solid solution with excellent oxidational behaviour. Due to a dense layer of aluminium oxide formed on the surface, oxygen diffusion is suppressed [4]. This material is termed titanium aluminium nitride. The incorporation of Al into the TiN matrix is possible up to a percentage of about 60-70 at.% of the metallic fraction. At higher percentages, the hexagonal wurtzite (w) aluminium nitride (AlN) phase occurs. If the Al content is further increased, the cubic phase disappears and w-AlN solid solution with incorporated Ti is formed [4]. Fig. 2.9a shows the TiN-AlN phase diagram for non-equilibrium processes. It can clearly be seen, that at elevated temperatures decomposition of the metastable solid solution to two phases takes place.

Another beneficial influence of the Al incorporation is an increase in hardness and Young´s modulus, as depicted in fig. 2.9b. A maximum is reached at an AlN concentration of approximately 50 at.%. Concentrations exceeding this value, however, result in decreasing hardness and Young´s modulus [39].

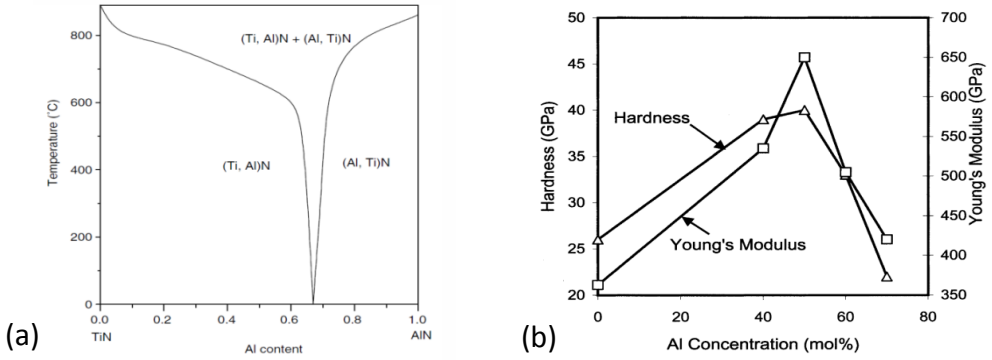

Fig. 2.9: Influence of the Al content on (a) the structural composition [40] and (b) hardness and Young´s modulus [39].

Using tantalum as an alloying element has proven to be beneficial for high temperature oxidation resistance and wear behaviour, because of a stabilisation of the fcc-phase. Thus, the lifetime of cutting tools can be significantly increased compared to non-alloyed TiAlN [41].

2.6 Residual Stresses

Residual stresses in thin films might originate because of various reasons such as [24]:

1. Substrate and film have different thermal expansion coefficients
2. Atoms might be incorporated at substitutional or interstitial lattice sites in the film
3. The lattice spacing is different for crystalline substrate and film during epitaxial growth
4. Alternating interatomic spacing with the crystal size
5. Recrystallization processes
6. Dislocations and microscopic voids

Very commonly the residual stresses are summarized as follows [9]:

$$\sigma^T = \sigma^i + \sigma^{th} \tag{2.1}$$

There σ^T determines the total residual stresses in the film, σ^i the intrinsic stresses and σ^{th} the thermal stresses. During physical vapour deposition, the film grows under highly non-equilibrium conditions. Therefore, compressive stresses are usually induced [5].

2.6.1 Thermal Residual Stresses

The thermal residual stresses are induced when the coated substrate is cooled down after deposition at elevated temperatures. They are depending on the thermal expansion coefficient of the substrate (α_s) and the coating (α_c). If α_c is higher than α_s, tensile stresses are induced into the coating when cooled down and vice versa [5]. The thermal stress component can be calculated by the following equation [5]:

$$\sigma^{\mathrm{th}} = \frac{\mathrm{E_c}}{1-\nu_c} \cdot (\alpha_s - \alpha_c) \cdot (\mathrm{T} - \mathrm{T_s}) \tag{2.2}$$

$\mathrm{E_c}$ and ν_c are the Young´s modulus and the Poisson's ratio of the coating, T is the actual temperature and $\mathrm{T_s}$ is the substrate temperature during deposition.

2.6.2 Intrinsic Residual Stresses

Intrinsic stresses are generated during the deposition process itself and are thus strongly depending on the conditions during deposition [5]. The stresses are generated in various ways. The most important factor influencing the intrinsic stresses, however, is high energetic ion bombardment [42]. A high-energy ion bombardment results in a higher number of defects. The energetic ions might occupy interstitial or vacant sites within the lattice as well,

which is leading to compressive stresses that can have a value of up to several GPa [5]. The bias voltage is strongly influencing the ion energy which is hence leading to a dependency of the stresses on the bias voltage [5,42,43].

2.6.3 Stress Relaxation

At temperatures exceeding deposition temperature, recovery of growth defects occurs spontaneously. This effect is driven by enhanced surface and bulk atom diffusion, which allows the atoms to reach their equilibrium positions, resulting in a densification of the film. This leads to a decrease of the compressive stresses [44].

Fig. 2.10 shows the typical stress-temperature dependence of coatings. In this case, the compressive stress increases during heating. The slope depends on the ratio of the thermal expansion coefficients of the film and the substrate. At temperatures above 550 °C, which was the deposition temperature in this case, stress relaxation occurs and the compressive stress decreases. While cooling, the stress is getting less and less until it even becomes approximately zero. The graph shows that the curves for heating and cooling are parallel, i.e. the thermal expansion coefficient is not influenced by stress relaxation [44].

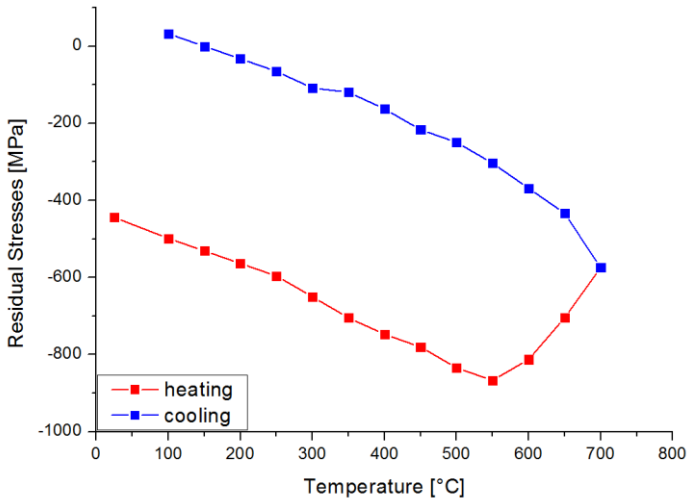

Fig. 2.10: Typical stress-temperature dependence curve of a sputtered chrome nitride coating with an onset temperature for stress relaxation of about 550 °C (own work).

2.7 Wafer Curvature Method

Deposition of a film on a flexible substrate results in a curvature due to the occurring residual stresses [45]. The origin of the stresses and the curvature is illustrated in fig. 2.11. If the film shrinks relative to the substrate, tensile stresses are induced in the film and a curvature is caused, see fig. 2.11a, and vice versa with expanding film (fig. 2.11b). This curvature can be used to determine the residual stresses. This was first done by Stoney in 1909 and nowadays it is commonly known as “wafer curvature method”. Stoney assumed the stresses to be uniaxial, however, today they are known to be biaxial which led to the development of the following modified equation [45]:

$$\sigma_c t_c = M \frac{{t_s}^2}{6R} \tag{2.3}$$

There, σ_c is the stress in the coating, t_c and t_s are the thicknesses of the coating and substrate, M is the biaxial modulus of the substrate and R is the bending radius of curvature of the initial flat substrate after deposition. As substrate, silicon single crystal wafers are regularly used, for which M is well known [45]. R is preferably measured by non-contact optical techniques, which have the advantage of not altering the surface as well as being sensitive [10].

Wafer curvature measurements are, compared to other techniques, such as lattice strain methods like e.g. X-ray diffraction, simply to perform because the instrumental afford is relatively low and amorphous coating materials can be investigated as well. On the other hand, they have the disadvantage of only providing an averaged data for the whole film [10].

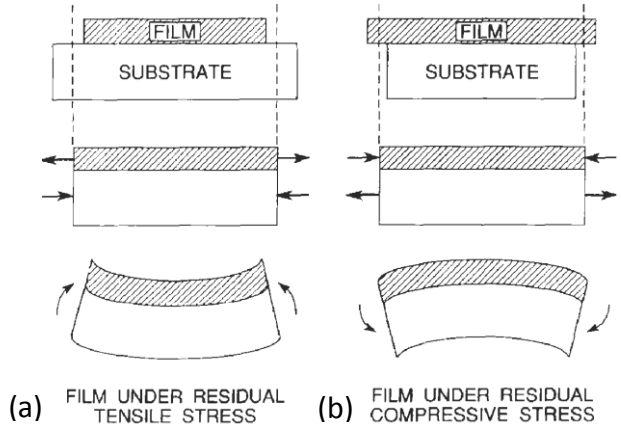

Fig. 2.11: Scheme of substrate deformation for (a) tensile and (b) compressive residual stresses [24].

3 Experimental Details

3.1 Coating Deposition

The coatings investigated within this thesis have been deposited by reactive unbalanced magnetron sputtering and reactive cathodic arc evaporation. The following section shortly summarizes the deposition methods and parameters used.

3.1.1 Sputter Deposition

The sputtered coatings were deposited by reactive magnetron sputtering in an industrial scale deposition plant of type CemeCon CC800® / 9MLT. This device is equipped with four bipolar pulsed DC magnetrons of size 500 x 88 mm². Four powder metallurgical titanium aluminium targets, produced by PLANSEE Composite Materials, Germany, were used for deposition. After a total pressure of less than 4 mPa was reached, a heating step was performed. Subsequently an Ar^+ ion etching step was carried out. After that, the actual deposition process was started. Two coatings with different unipolarly pulsed bias voltages of -40 and -50 V, respectively, were deposited, using a pulse frequency of 350 kHz and a reversal time of 1000 ns. The deposition time for each coating was 255 minutes at a deposition temperature of approximately 550 °C. The argon flow was set constant to 200 sccm, while the pressure during deposition was controlled to 580 mPa by the nitrogen flow. The cathode power was set to 7000 W for each cathode and was pulsed with a frequency of 50 kHz.

3.1.2 Cathodic Arc Evaporation

The arc evaporated coatings were deposited in an industrial scale cathodic arc evaporation facility, type Oerlikon Balzers INNOVA. Six powder metallurgically produced targets were used during each deposition. The targets had a different composition for each coating. Prior to the actual deposition process, the facility was evacuated to a pressure of less than 1 mPa. After that, a heating step and an etching step with argon ions were performed. The bias voltage for all coatings was set to -40 V and the deposition time was 250 minutes. The depositions were performed at a temperature of 550 °C in a pure nitrogen atmosphere, having a pressure of 3.2×10^{-2} mbar.

3.1.3 Comparison of the Deposited Coatings

Table 3.1 gives an overview of the coatings investigated within this thesis. The names of the coatings are composed of a letter and a number. The letter indicates the process used to deposit the coating, where the capital letter S stands for sputtering and A for arc evaporation. The number behind the letter indicates the bias voltage for the sputtered coatings and the chemical composition of the targets for the arc evaporated coatings, respectively.

Tab. 3.1: Target composition and bias voltage of the deposited coatings.

Coating	**S_40**	**S_50**	**A_50/50**	**A_50/50/1**	**A_33/67**	**A_32/63/5**
Deposition process	sputtering		arc-evaporation			
Target composition [at.%]	Ti/Al/Ta					
	40/60/0	40/60/0	50/50/0	49.5/49.5/1	33/67/0	31.7/63.3/5
Bias voltage [V]	-40	-50	-40			

3.1.4 Substrate

As substrate single crystal silicon strips in (100) orientation, with a dimension of 7 x 21 mm² and a thickness of 380 and 500 µm, respectively, were used. The biaxial modulus used in the calculation of the stresses was 180 GPa [45]. Prior to deposition, they were cleaned in acetone and ethanol for ten minutes each.

3.2 Coating Characterization

3.2.1 Ball Crater Technique

The coating thickness was determined by the so called ball crater technique. A steel ball with the diameter D_0, covered with diamond paste is driven by a notched shaft, rotating on the surface of the coated substrate. Thus, a spherical calotte is grinded into the material according to fig. 3.1a. Pictures of the resulting craters were taken using an optical Reichert-Jung microscope of type Polyvar Met with an attached CCD camera, see fig. 3.1b. The resulting diameters D and d were measured using the software analySIS®.

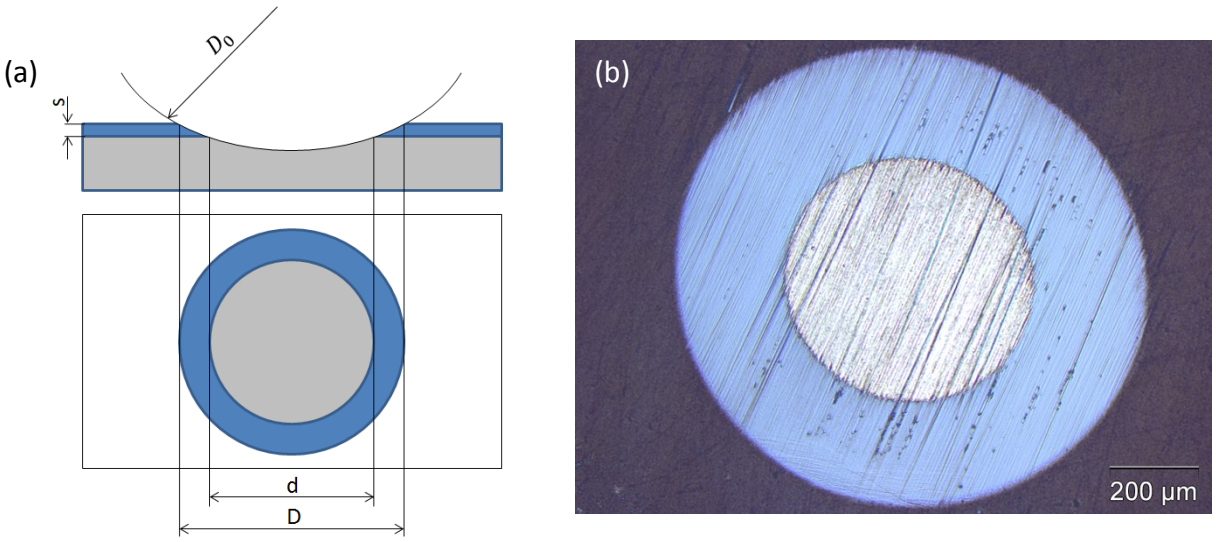

Fig. 3.1: Schematic of the ball crater technique (a) and an image taken with the optical microscope, subsequently used to determine the coating thickness (b) (own work). The necessary diameters for calculation are depicted in (a).

The coating thickness can thus be calculated by the following equation [46]:

$$s = \frac{D^2 - d^2}{4D_0} \tag{3.1}$$

3.2.2 Scanning Electron Microscope

The chemical composition of the coatings was analysed by energy dispersive X-Ray emission spectroscopy (EDX) using a Zeiss Auriga scanning electron microscope (SEM) equipped with an Apollo 40+ EDX-Detector. One specimen for each type of coating was investigated.

3.2.3 X-Ray Diffraction

X-Ray Diffraction (XRD) was applied to determine the crystal structure of the coatings using a Bruker-AXS D8 Advance diffractometer. All measurements were carried out in gracing incidence configuration using copper K_α radiation. The tube voltage was set to 40 kV and the tube current was 40 mA. The inclining angle of the X-ray tube was 2°. Each coating was scanned from 20 – 85° with a step size of 0.02° and a time of 1.2 sec for each step.

3.2.4 Nano Indentation

A UMIS (Ultra Micro Indentation System) nano indenter from Fischer-Cripps Laboratories, equipped with a Berkovich indenter [47], was used to determine the hardness and the Young´s modulus of the coatings. A plateau test, from 25 to 1 mN in steps of 1 mN, was carried out for each coating. To exclude the possibility of an influence of surface irregularities, the samples were carefully polished before measurement. The obtained data was analysed using the software IBIS provided by the manufacturer. To achieve reasonable statistics, at least ten indents of each sample were used for analysis.

3.2.5 Infrared Camera

For the thermographic measurements of the heating plate, an infrared camera type Titanium SC 7500MB provided by FLIR® was used. This camera is equipped with an indium antimonide (InSb) detector, with a resolution of 640 x 512 pixels, and a maximum frame rate of 100 Hz. The analysis of the data was carried out with the provided software AltaIR, which allows communication between PC and camera. The setup during measurement is depicted in fig. 3.2.

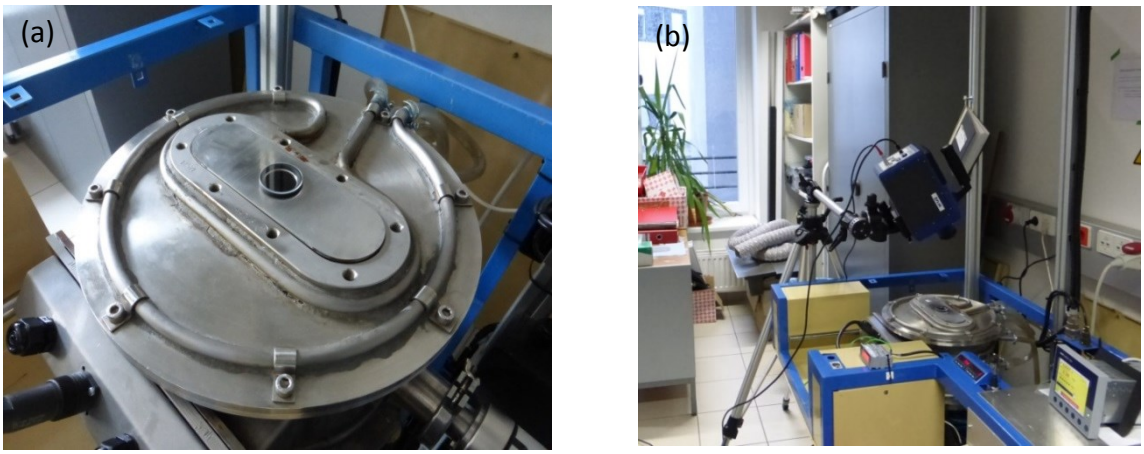

Fig. 3.2: Setup during infrared measurement, (a) vacuum chamber with steel plate and infrared transparent barium fluoride glass, (b) infrared camera positioned over the vacuum chamber on a tripod.

The thermographic measurements were carried out in cooperation with the chair for automation, to determine the actual temperature and the temperature distribution of the heating plate and the samples. Usually a quartz glass is used for the biaxial stress temperature measurements (BSTM). However, it is not transparent for electromagnetic waves with a higher wave length than approximately 2 µm [48]. As barium fluoride (BaF_2) is transparent for infrared radiation up to a wavelength of 10 µm [49], a round BaF_2 glass, with a diameter of 49 mm, was used instead. A steel plate with a 30 mm hole in the middle was used to cover the opening that is usually covered by the quartz glass. The BaF_2 glass is placed on the hole, connected by a 35 mm sealing ring to preserve the vacuum.

3.2.6 Wafer Curvature Measurements

The wafer curvature measurements were carried out using the BSTM device “Mutti 2000”, constructed by Winkler [50], which can be seen in fig. 3.3. The samples are placed in a vacuum chamber (a) to protect them from oxidation at elevated temperatures. On its top, a removable glass plate is located, through which the samples are fed onto the heating plate. For measurements at room temperature the samples can alternatively be positioned directly onto the glass. The vacuum is supplied by a Pfeiffer DUO 10M backing pump (b), and a HiPACE turbo pump located under the vacuum chamber.

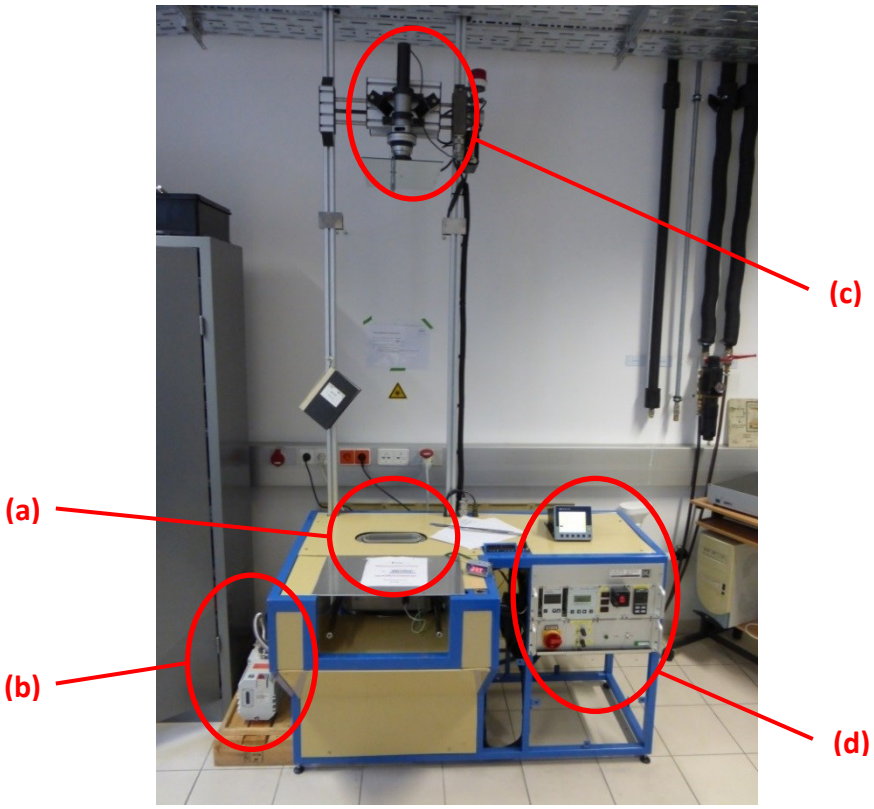

Fig. 3.3: BSTM apparatus “Mutti 2000”; (a) removable glass window, (b) vacuum pump, (c) laser unit, (d) control unit.

To measure the radius of the specimen, two parallel beams provided by a laser and a beam splitter attached on the top of the device are used (c). The principle of the measurement is depicted in fig. 3.4. The laser beams have a known distance and are projected onto the sample from above. They are reflected on the upside of the specimen to a mirror, where they are reflected again onto the measuring plate. The distance between the laser spots after reflection is proportional to the deflection of the coated samples. With the given distances d_o, h_1 and h_2, the radius R of the deflected specimen can be calculated by solely measuring the distance d_1, using the following equation [51]:

$$R = \frac{2\cdot(h_1+h_2)\cdot d_0}{d_0-d_1} \tag{3.2}$$

The internal stresses were then calculated using the modified Stoney equation (2.3). M is the biaxial modulus of (100) oriented silicon $M_{(100)}$ = 180 GPa [45], which was used as substrate for the measurements performed in this thesis. The measurements were carried out in high vacuum and at temperatures between room temperature and 600°C.

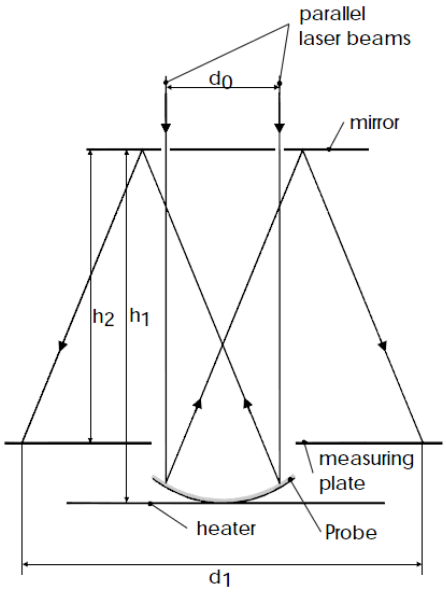

Fig. 3.4: Principle of the deflection measurement by two parallel laser beams, as used in the "Mutti 2000" BSTM system [51].

3.2.7 Metal Melting Test

In order to verify the temperatures given by the above mentioned thermocouple, a metal melting test was carried out. Three different metals were positioned on different silicon strips in the vacuum chamber. The used metals were chosen with respect to their melting temperature, which should be between 100 and 500 °C. They are given with their melting point in table 3.2. It was assumed that the pressure of the atmosphere does not have an influence on the melting temperature of the metal, thus the tests were performed in vacuum, in order to prevent the metals from oxidation. Additionally, they should not form low melting compounds with silicon. This was ensured by considering the phase diagrams for indium [52], tin [53] and lead [54].

Tab. 3.2: Metals chosen for the melting test with their melting temperatures [55].

Metal	**Indium (In)**	**Tin (Sn)**	**Lead (Pb)**
Melting temperature [°C]	156.4	231.8	327.0

4 Results and Discussion

4.1 BSTM Heating Device

Wafer curvature measurements may induce a comparatively large experimental error compared to lattice strain methods. Thus, it is very important to provide a homogenous temperature distribution and reproducible conditions during measurement. However, this demand could not be satisfyingly fulfilled by the heating device installed on the existing BSTM apparatus. The original device used two 1000 W filament lamps, irradiating the specimen from underneath. This led to significant temperature differences, depending on whether the specimen was positioned directly over a lamp, between the lamps or laterally displaced.

An alternative was found in a silicon nitride full-ceramic heating plate type SCD from Bach Resistor Ceramics GmbH, see fig. 4.1. The heating plate has an extension of 100 x 100 mm² and is equipped with two symmetrically arranged heating circles, with a maximum power of 2000 W each and a maximum operating temperature of 1000 °C. The plate has two drilled holes on its underside having a diameter of 1 mm. They are located in the centre of the plate, and laterally displaced between the two heating circles. Two type K thermocouples with a diameter of 1 mm were inserted for temperature measurement.

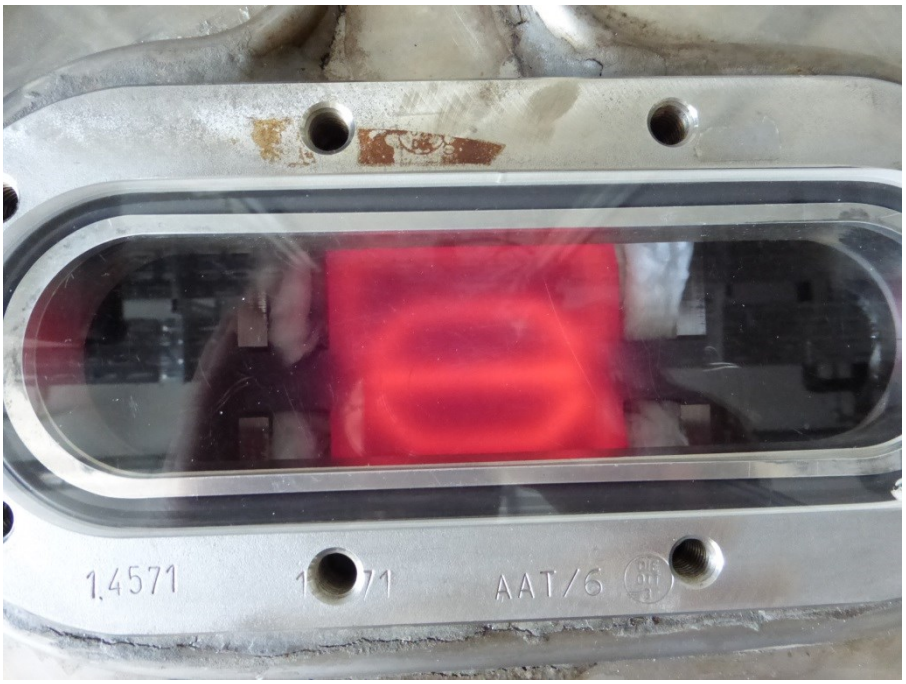

Fig. 4.1: Photography of the heating device in the vacuum chamber during heating; the two 2000 W heating circles can be recognized as gleaming lines.

Due to the new heating device, a new mounting system had to be designed as well. The mounting system is displayed in fig. 4.2. It basically consists of a steel frame with two notches on the sides, where the heating plate is connected to the power supply. The frame is screwed onto a T-shaped steel bar, which is mounted to the front panel of the vacuum chamber by six steel screws. By adjusting the two interior screws, the horizontal plane can be tilted. By opening the four screws which connect the steel frame with the T-bar, the heating plate can be shifted into horizontal direction, within the range of four elongated holes.

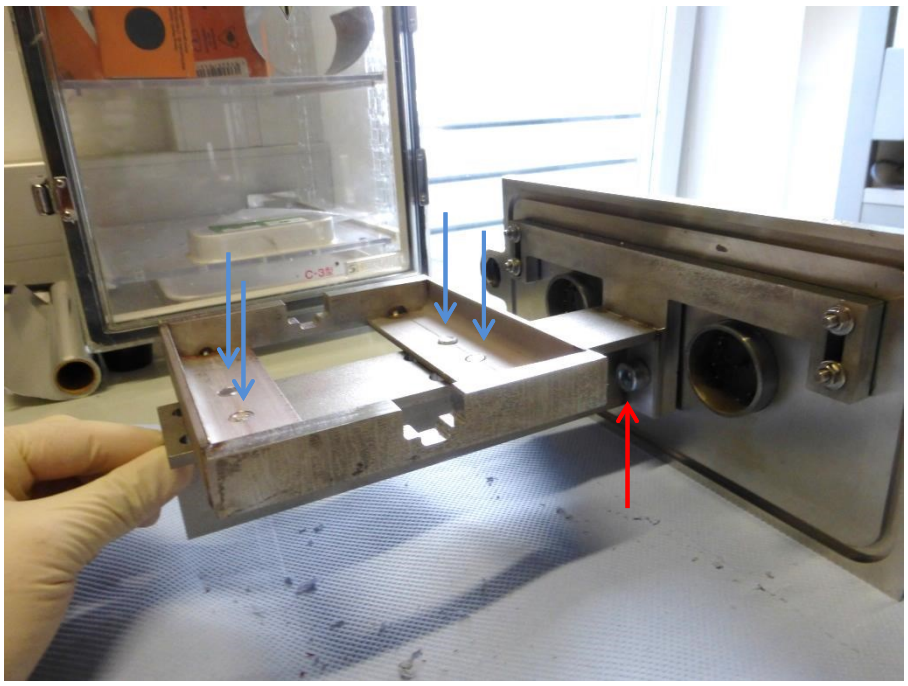

Fig. 4.2: Mounting system for the heating plate. The location of the screws for tilting the plate are indicated with a red arrow and the screws for shifting the plate are indicated with blue arrows.

The steel frame is lined with fibre glass mats, onto which the heating plate is placed. This is done in order to *(i)* insulate the steel frame against the emitted heat and to *(ii)* guarantee a soft, protecting underground for the ceramic heating plate. Additionally, an adjustment of the horizontal orientation of the heating plate can be performed by the amount of glass fibre which is used.

During the measurement, the samples are placed next to each other directly onto the heating plate, over the central heating section. Thus, constant temperature for all samples is guaranteed, which leads to reproducible and comparable measurements. Up to four or even five samples can be measured at once.

4.1.1 Controller Calibration

Because the heating plate has two separate heating circles, a JUMO IMAGO 500 multichannel controller is used to adjust the temperature [56]. This device can handle up to eight channels at once and has a digital interface for operation. The basic principle of the control unit is shown in fig. 4.3. The JUMO IMAGO 500 is fed with the information from one thermocouple attached underneath the heating plate. The output signal ranges from 4 to 20 mA which refers to 0 and 100 % power, respectively. The two signals are linked to each other, thus both heating circles are heated with the same power. Two thyristor controllers type AEG Tyro 1A convert the information into equivalent operating voltages that supply the heating plate. A protective switch is connected between the thyristors and the heating plate which receives the pressure information from the pressure gauge in the form of an electric signal. It disconnects the heating device from the power if the pressure is above 10^{-3} mbar, in order to avoid a plasma discharge between the contacts, which might ignite in a certain pressure range.

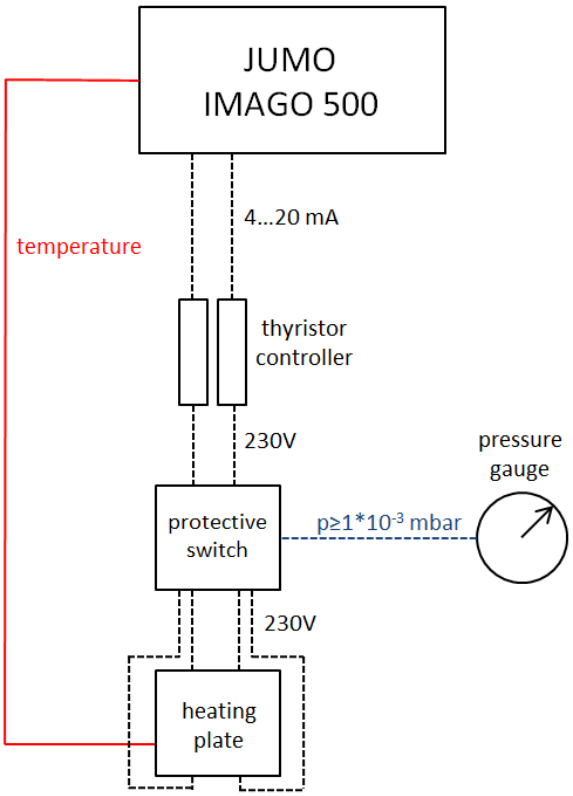

Fig. 4.3: Principle of the information flow in the control unit of “Mutti 2000”.

In order to obtain fast and exact heating and cooling, an optimisation of the control parameters was carried out. The parameters that were adjusted are the reset time (Tn), derivative time (Tv), proportional band (Xp) and cycle time (Cy). Fig. 4.4 shows the influence of the different parameters on the heating curve.

If the parameters are ideally adjusted, the actual value approaches directly the set temperature, see fig. 4.4f. If the proportional band is too large or the derivative and reset time are too small, an overshooting actual temperature is the consequence, which results in a longer settling time (fig. 4.4a and b). On the other hand, if the proportional band is too small and the derivative and reset times are too large, the temperature does not reach the set value during the first heating, which causes a longer settling time as well, see fig. 4.4d and e. A too large cycle time causes a periodical oscillation along the set temperature, see fig. 4.4c.

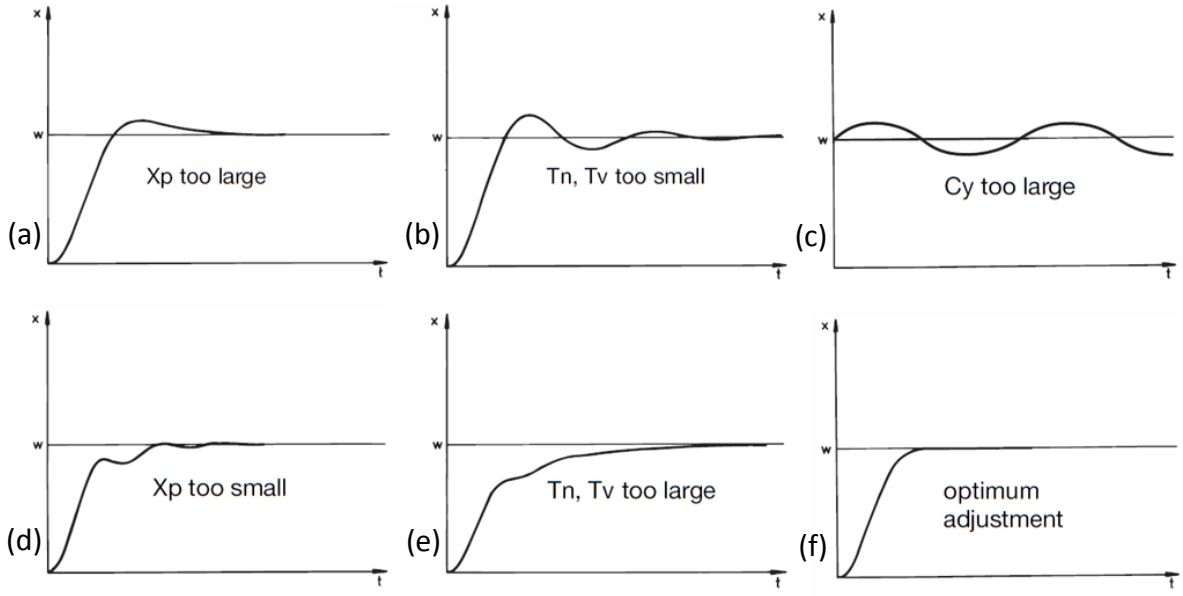

Fig. 4.4: Influence of adjustable control parameters on the heating curve, X indicates the controlled variable, t is the time and w is the set value [56].

The four parameters were varied within the values given in table 4.1. The temperature curve was qualitatively analysed with respect to settling time, heating rate, cooling rate and temperature overshoot for different set temperatures. Consequently, the best parameter compilation was chosen as standard setup.

Tab. 4.1: Summary of the minimal and maximal value, between which the parameters were varied.

	Reset time [sec]	**Derivative time [sec]**	**Proportional band [-]**	**Cycle time [sec]**
Minimal value	20	10	300	10
Maximal value	300	60	550	60

A compromise between a low settling time for heating and cooling needed to be found, which led to the parameters given in table 4.2. While heating, the settling time is approximately 2 to 4 minutes for the finally set parameters, depending on the difference between actual temperature and set temperature. The overshoot was minimized to 5 °C at low temperatures and approximately 8 to 9 °C for higher temperatures.

Tab. 4.2: Summary of the control parameters finally set after variation.

Reset time [sec]	Derivative time [sec]	Proportional band [-]	Cycle time [sec]
175	16	550	60

The settling time during cooling depends strongly on the temperature level. At elevated temperatures above approximately 300 °C, the cooling rate is very high and therefore controlling is necessary. It is important to minimize the undershoot during cooling in this range in order to obtain a short settling time. In contrast to that, at low temperatures the cooling rate is also low; it is not necessary to control the temperature anymore and measurements can be carried out directly during cooling.

4.1.2 Temperature Discrepancy

A very challenging issue within this thesis was to determine the temperature of the samples. It was found, that the difference between the temperature of the heating plate and the silicon specimens is rather large. It cannot be assumed that they have the same temperature as the heating plate. Therefore, it was necessary to carry out further investigations in order to obtain satisfying values for the sample temperature.

4.1.2.1 Thermographic Measurements

One thermographic measurement was performed continuously between room temperature and 700 °C. Two coated silicon samples were placed in the chamber, which was then heated. One sample was placed with the coated side downwards; the other one faced the coated side upwards. In fig. 4.5a the image taken from the infrared camera for a set temperature of 600 °C is depicted. Bright areas indicate a field of higher temperature, whereas dark areas refer to fields with lower temperature. It can be seen that the temperature on the heating plate is homogenous. For the area outside the samples, no recognisable temperature difference can be seen. This indicates that the thermal conditions are equal for all samples. However, fig. 4.5a also suggests that the temperature of the silicon strips is significantly lower than the temperature of the heating plate. This is also shown in the profiles depicted in fig. 4.5b.

Fig. 4.5b shows that the temperature of the heating plate correlates well with the temperature set on the controller. It has a temperature of 600 °C, which is exactly the set temperature. The maximum difference between heating plate and sample, however, is somewhat high; 140 °C for the right sector of profile 14. Another surprising result is that the temperature seems to be not constant over the whole sample. The profiles show that on the right sample a temperature difference occurs. The reason might be the infrared radiation that is sent out by the heating plate. It is reflected within the chamber and again by the sample surface. Therefore, a higher temperature, than the actual one is measured.

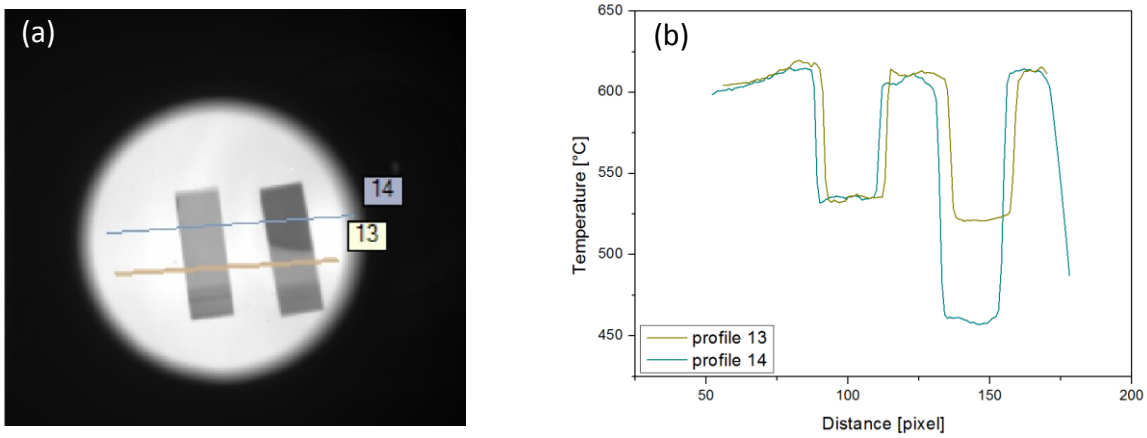

Fig. 4.5: (a) Image taken from the infrared camera for a set temperature of 600 °C. The left sample has the coated side faced downwards the right one upwards (b). Two line scans were placed over the samples, indicated with 13 and 14. The emissivity was assumed to be 0.95.

This interpretation is supported by a second test that was done, whose result for 350 °C is depicted in fig. 4.6. During this test a silicon sample was positioned between two samples coated with aluminium oxide. The aluminium oxide has a black and matt surface whereas the silicon surface is bright and shiny. Reflections can very clearly be seen on the inner silicon strip. The temperature varies within approximately 40 °C and is therefore not constant over the sample. In contrast to that, the outer, coated strips reflect the radiation with a much smaller amount. Therefore, the measured temperature is lower and more homogenous. The test also shows that the temperature at 350°C correlates well with the set temperature.

Due to the high temperature difference between heating plate and samples, the temperature set at the controller cannot be assumed to be the same for the samples. Therefore, an additional thermocouple was installed which determines the temperature on the surface of a silicon strip. This additional strip is positioned next to the samples that are intended for actual measurement.

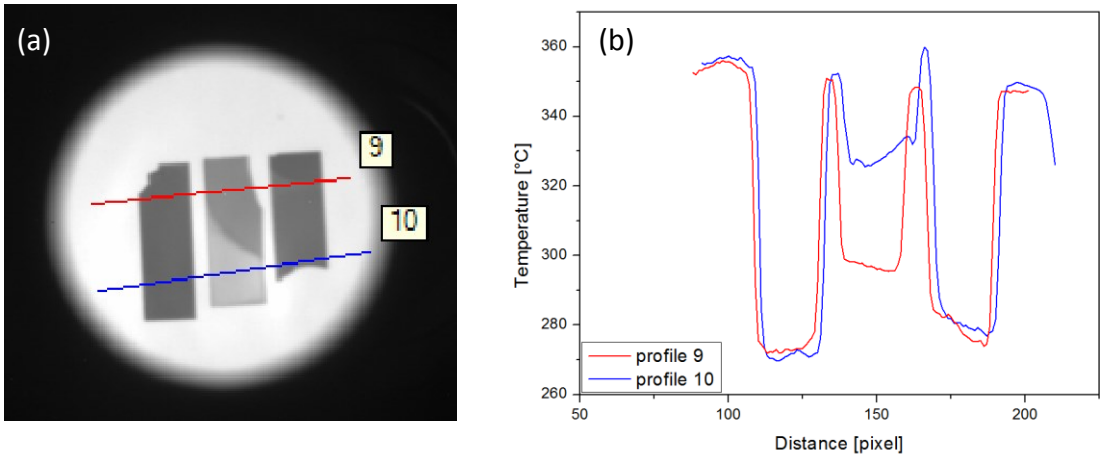

Fig. 4.6: (a) Picture and (b) profiles of a silicon sample in the middle of two aluminium oxide samples at a set temperature of 350 °C.

4.1.2.2 Metal Melting Test

To validate the temperature given by the above mentioned thermocouple, the melting points of selected reference metals placed on top of silicon strips was measured. Fig. 4.7 shows the results of the melting test. It can be seen, that there is a difference between the melting points of the metals and the measured temperatures, i.e. the thermocouple measures a value that is lower than the actual one. The reason might be the fact, that the heat transfer to the thermocouple is not ideal. A certain loss of heat occurs, resulting in the lower temperature at the tip of the thermocouple. The difference is approximately 30 °C and is to a certain degree the same for all metals and is thus assumed to be constant over temperature. Therefore, in the following all measured values above 100 °C were corrected by an addition of 30°C, which results in a general temperature accuracy of ± 10 °C.

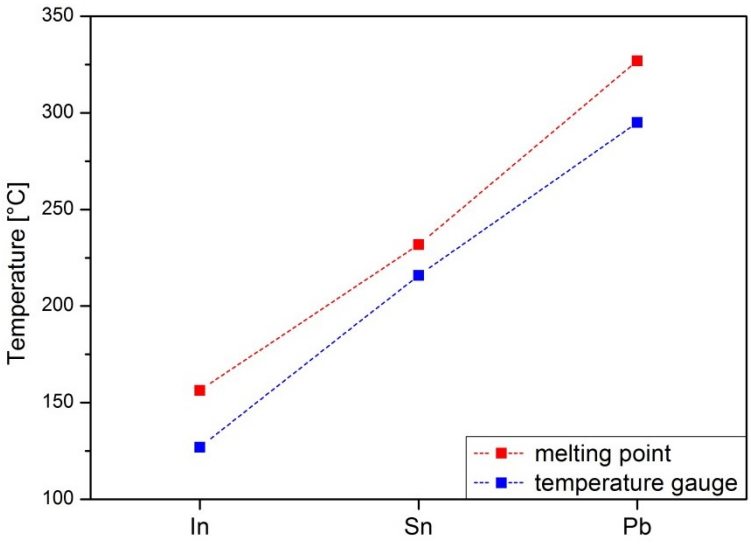

Fig. 4.7: Difference between measured temperature and the melting point of the three investigated metals.

4.1.2.3 Condition Variation

In order to evaluate the origin of the temperature discrepancy, the conditions for the samples have been varied. The temperature of the samples was measured as a function of the set temperature of the heating plate. The results depicted in fig. 4.8 show that in general the difference between sample temperature and set temperature is increasing with increasing temperature. While at low temperatures around 100 °C the difference is only 30 °C, at higher temperatures about 900 °C it grows up to a difference of approximately 300 °C. A possible reason might be that the heat transfer between heating plate and sample is low. Due to the applied vacuum, no heat transfer through convection can take place, which results in a lower temperature. This assumption is supported by the fact, that by executing the measurements in a ventilated chamber, i.e. at ambient pressure, the temperature can be increased by approximately 50 °C. However, a disadvantage is that at elevated temperatures, oxidation of the electronic contacts of the heating plate might take place. Therefore, it is not advisable to perform measurements at set temperatures higher than 500 °C in a ventilated chamber. Hence, no yield in temperature is obtained.

Additionally it was observed, that there is negligible temperature difference between placing the sample with the coated side upwards or downwards, respectively. Therefore, the sample can be positioned both ways without the necessity of applying any further correction during analysis.

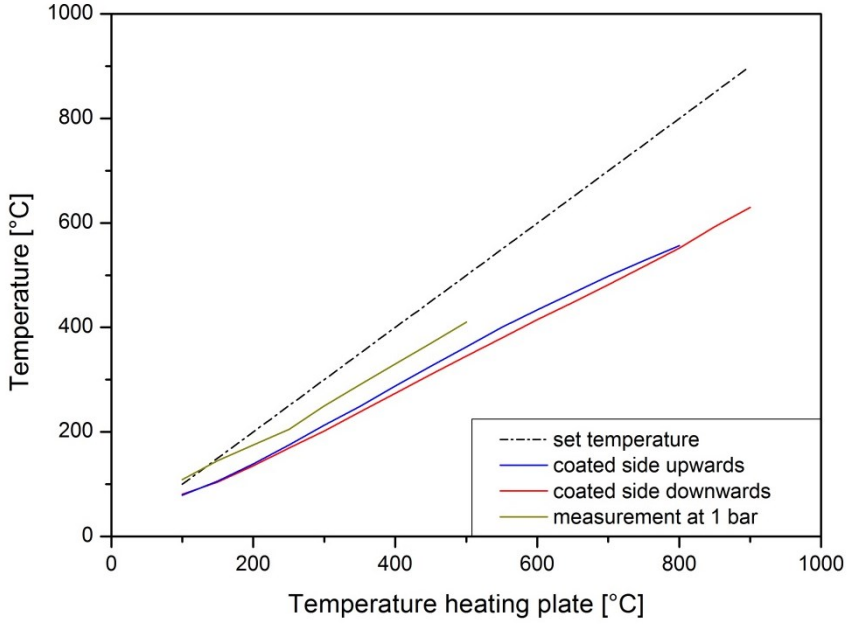

Fig. 4.8: Temperature difference between set temperature and differently conditioned samples.

4.2 Coating Properties

4.2.1 Chemical Composition

The chemical composition of each coating was determined by EDX and is shown in table 4.3. For the sputtered coatings the exact target composition is not known. The composition of the metallic fraction of the coating, however, was determined to be 40 at.% titanium and 60 at.% aluminium. The arc evaporated coatings A_50/50/1 and A_32/63/5, see table 3.1, showed an increased Ta content compared to the target composition, whereas the Al content is slightly decreased. For the other two arc evaporated coatings, the target and coating composition do not differ.

Tab. 4.3: Composition of the targets and coatings with respect to the metallic fraction.

Coating	S_40	S_50	A_50/50	A_50/50/1	A_33/67	A_32/63/5
	Ti/Al/Ta [at.%]					
Target composition	-	-	50/50/0	49.5/49.5/1	33/67	31.7/63.3/5
Coating composition	40/60/0	40/60/0	50/50/0	49/48/3	33.3/66.7/0	31.6/58.7/9.7

4.2.2 Coating Thickness

The coating thickness was determined using the ball crater technique, which is described in section 3.2.1. The results are given in table 4.4.

Tab. 4.4: Coating thickness of the investigated coatings.

Coating	S_40	S_50	A_50/50	A_50/50/1	A_33/67	A_32/63/5
Coating thickness [µm]	5.4	5.4	6.3	5.1	6.3	7.0

The thickness of the arc evaporated coatings varies between 5.1 and 7 µm. The sputtered coatings have both the same thickness of 5.4 µm.

4.2.3 Crystallographic Structure

The XRD patterns for all coatings are shown in fig. 4.9. The patterns look similar for the sputtered and the arc evaporated coatings with 50 at.% aluminium and 50 at.% titanium (a-d). In fig. 4.10, the pattern of the sputtered coating S_40 is depicted and the standard peak positions for fcc-TiN (ICDD 00-038-1420) and fcc-AlN (ICDD 00-025-133) are indicated. As the coatings are a solid solution of fcc-TiN and fcc-AlN, the measured peaks of the coating are positioned directly between the indicated peaks, which is in good agreement to Vegard´s law [57]. No evidence for an additional crystalline phase could be found in the diffractogram.

For the other two arc evaporated coatings, with the raised aluminium content, the XRD patterns look different to the others, see fig. 4.9e,f. Fig. 4.11 shows the pattern of the A_32/63/5 coating, with the standard peaks indicated for cubic AlN and TiN and hexagonal AlN (ICDD 00-025-1133). The structures of these coatings consist of cubic and hexagonal parts. The peaks detected at 43 and 63° can clearly be related to the cubic (100) and (110) orientations. On the other hand, at 34 and 70° peaks referring to a hexagonal phase can be observed. This result agrees well with the investigations of Pfeiler *et* al. [41], who determined a mixture of cubic and hexagonal structures as well for arc evaporated coatings with high Al content.

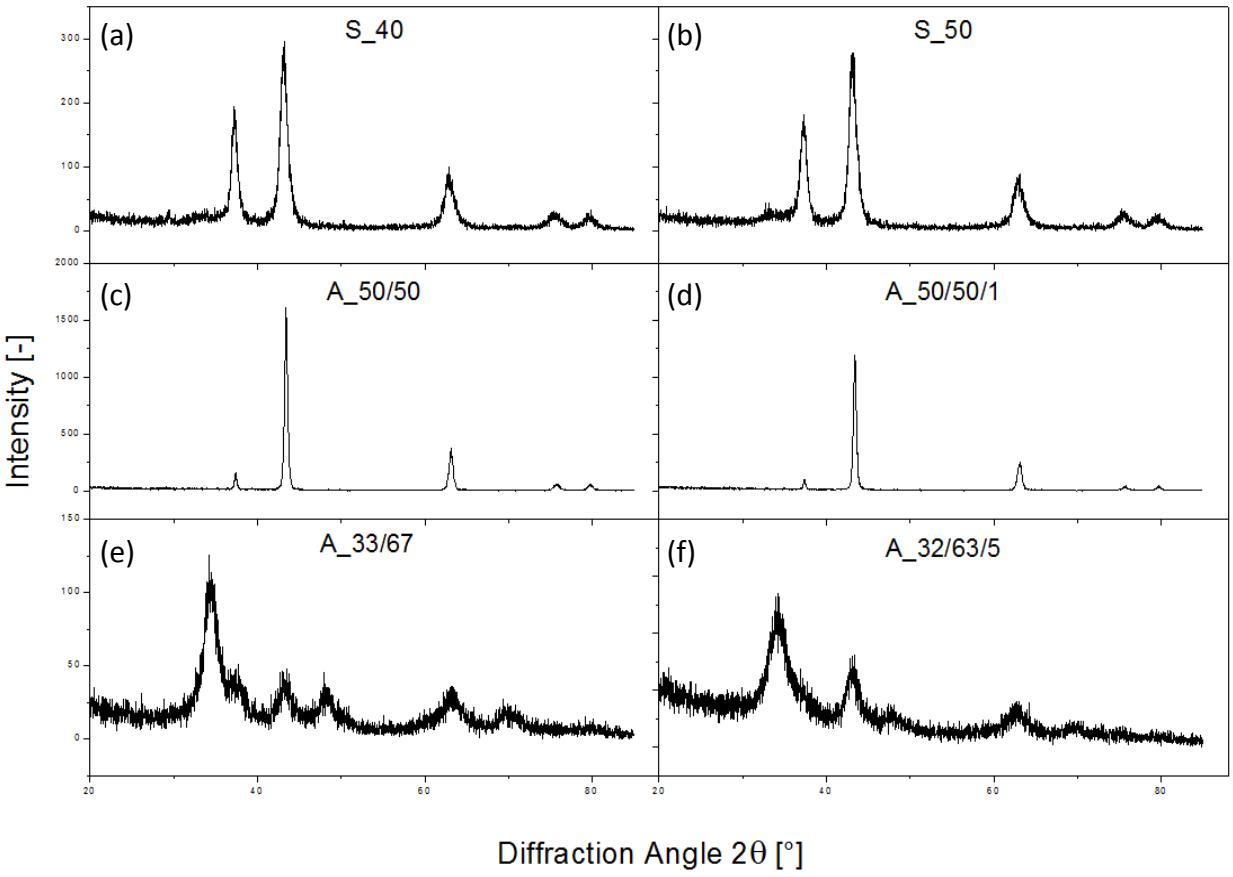

Fig. 4.9: XRD diffractograms of the investigated sputtered and arc evaporated coatings.

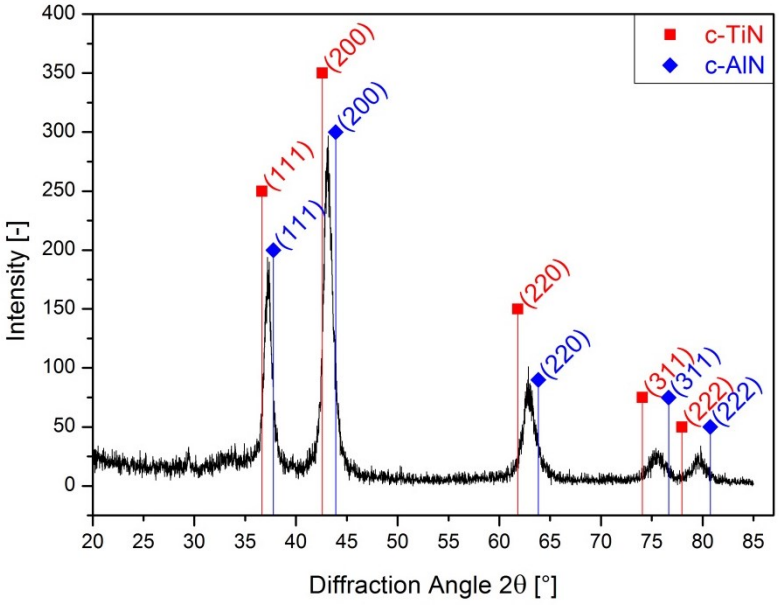

Fig. 4.10: XRD diffractogram of the sputtered coating S_40 with the peak positions for cubic TiN and AlN.

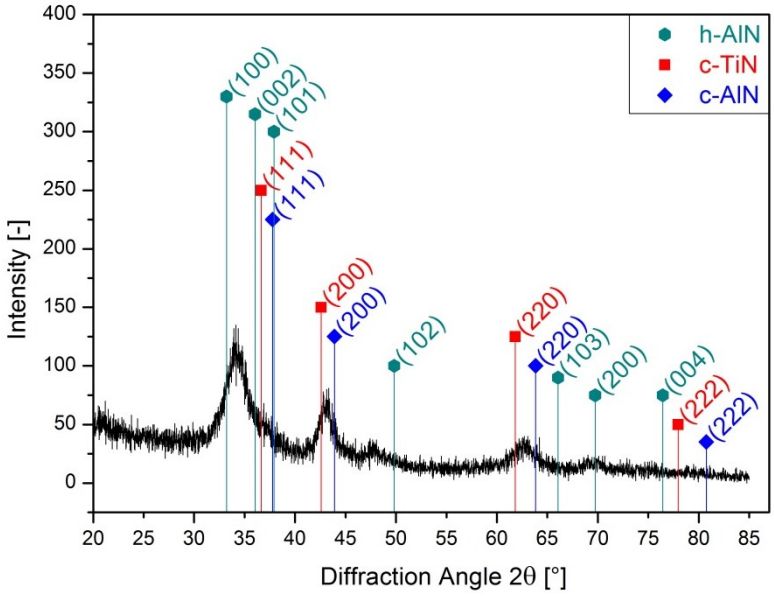

Fig. 4.11: XRD diffractogram of the arc evaporated coating A_32/63/5 with the peak positions for cubic AlN and TiN, and hexagonal AlN.

4.2.4 Mechanical Properties

Hardness and Young´s modulus of the coatings were determined using a UMIS nano indenter. The results are summarized in table 4.5. The hardness of the coatings is in the range of ~ 22 to 29 GPa. At higher aluminium contents, the formation of a hexagonal phase takes place. This leads to a lower hardness of the coatings A_33/67 and A_32/63/5, compared to the other arc evaporated and sputtered coatings. A similar tendency can be seen for the Young´s modulus. It is reduced for those two coatings as well, to a value of less than 300 GPa. This correlates well with the observations of PalDey *et* al. [39]; the mechanical

properties are decreasing at Al contents above 50 at.%, see fig. 2.9b. This can be related to the crystallographic structure, which is a mixture of cubic and hexagonal phases [58], described in the previous section.

The mechanical properties also indicate that tantalum affects the coating hardness. The hardness is increased in the coatings A_50/50/1 and A_32/63/5 compared to the Ta-free coatings A_50/50 and A_33/67. The reason is that Ta stabilizes the cubic phase, which results in beneficial mechanical properties [59].

The bias voltage does not have an important influence on the Young´s modulus. There is no significant difference between the coating S_40 and S_50. Remarkably, the measured hardness is lower for the coating with the higher bias voltage. This is contrary to the assumptions stated in literature [41,60].

Tab. 4.5: Hardness and Young´s modulus of the investigated coatings.

Coating	S_40	S_50	A_50/50	A_50/50/1	A_33/67	A_32/63/5
Hardness [GPa]	27.8 ± 2.4	25.8 ± 4.4	27.6 ± 5.7	28.8 ± 2.5	21.7 ± 2.2	22.9 ± 2.8
Young´s modulus [GPa]	424 ± 20	432 ± 33	470 ± 78	457 ± 39	244 ± 16	272 ± 17

4.2.5 Residual Stress at Room Temperature

The residual stress at room temperature is given in table 4.6. Similar to the mechanical properties, tantalum raises the value of the residual stress, compared to the coatings without Ta. The differences for the coatings A_50/50/1 and A_32/63/5 are significant; the difference between A_50/50 and A_50/50/1, which is doped with approximately 3 at.% tantalum, is 300 MPa. The bias voltage has a remarkable influence as well, agreeing with the observations of Chu *et* al. [61]. By increasing the bias voltage from -40 to -50 V, the stresses are raised by more than 200 %.

Tab. 4.6: Residual stress at room temperature.

Coating	S_40	S_50	A_50/50	A_50/50/1	A_33/67	A_32/63/5
Residual stress at room temperature [MPa]	-498 ± 280	-1763 ± 501	-505 ± 19.0	-817 ± 24.0	-419 ± 10.4	-559 ± 19.1

4.2.6 Thermal Expansion Coefficient

The thermal expansion coefficient was determined by wafer curvature measurements. To calculate the thermal expansion coefficient, eq. (2.2) was used. In order to obtain the Young´s modulus of the bulk coating $E_{c,b}$, which is necessary for calculations, the modulus E_c obtained by nano indentation was corrected by multiplication with $(1-\nu_c^2)$. For stresses at two different temperatures, the equation reads as follows:

$$\sigma_1^{th} = \frac{E_{c,b}}{1-\nu_c} \cdot (\alpha_s - \alpha_c) \cdot (T_1 - T_s) \quad (4.1)$$

and:

$$\sigma_2^{th} = \frac{E_{c,b}}{1-\nu_c} \cdot (\alpha_s - \alpha_c) \cdot (T_2 - T_s) \quad (4.2)$$

Subtracting eq. (4.2) from (4.1) and dividing by the temperature difference $T_1 - T_2$ leads to the following equation:

$$\frac{\sigma_1^{th} - \sigma_2^{th}}{T_1 - T_2} = \frac{E_{c,b}}{1-\nu_c} \cdot (\alpha_s - \alpha_c) = \frac{\Delta\sigma}{\Delta T} \quad (4.3)$$

$\frac{\Delta\sigma}{\Delta T}$ equals the slope of the measured curve. Transforming eq. (4.3) yields the following expression for the thermal expansion coefficient α_c:

$$\alpha_c = \alpha_s - \frac{\Delta\sigma}{\Delta T} \cdot \frac{1-\nu_c}{E_{c,b}} \quad (4.4)$$

α_s is the expansion coefficient of the silicon substrate which has a value of 2.6 x 10^{-6} K^{-1} [5]. The slope was determined by a linear approximation using the OriginPro 8.5G program, see the example depicted in fig. 4.12. The values for the Poisson´s ratio of the coating ν_c in literature vary between 0.3 [62] and 0.143 [63]. Hence, the Poisson´s ratio was assumed to be 0.25, which is an intermediate value.

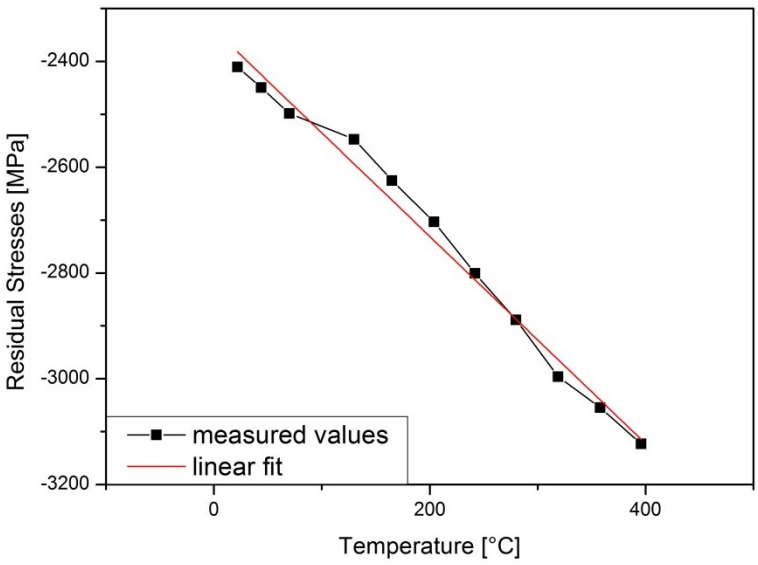

Fig. 4.12: Example of a linear fit that was used to determine the thermal expansion coefficient of the coatings.

For each coating, three different samples were measured in order to obtain reasonable statistics. The thermal expansion coefficients were calculated and averaged; the results are given in table 4.7.

Tab. 4.7: Thermal expansion coefficients of the investigated coatings.

Coating	S_40	S_50	A_50/50	A_50/50/1	A_33/67	A_32/63/5
Thermal expansion coefficient 10^6 [K^{-1}]	6.59 ± 0.34	6.27 ± 0.41	5.89 ± 0.07	6.82 ± 0.06	5.54 ± 0.10	5.06 ± 0.09

The thermal expansion coefficients obtained from measurements have a value between the thermal expansion coefficients for hexagonal AlN and cubic TiN, which are 4.5 x 10^{-6} K^{-1} [64] and 9.4 x 10^{-6} K^{-1} [65], respectively. It is obvious that the bias voltage does not have a significant influence on the thermal expansion coefficient; the values for S_40 and S_50 are within the range of the standard deviation. No clear tendency of the effect of tantalum can be observed either. On the one hand, the thermal expansion coefficient of the coating A_50/50/1 is raised compared to A_50/50, but on the other hand it is decreased for A_32/63/5, compared to A_33/67. The values given in table 4.7 also show that the coatings A_33/67 and A_32/63/5 have a thermal expansion coefficient that is lower, compared to the other ones. The reason might be that those two coatings do not have a completely cubic structure, but contain a recognisable fraction of hexagonal phase as well, which is indicated by the XRD patterns in section 4.2.3. Thus, the thermal expansion coefficient is closer to the value for hexagonal AlN.

4.3 Stress-Temperature Behaviour

4.3.1 Non-Isothermal Tests

In order to determine the stress-temperature behaviour of the coatings, their curvature was measured as a function of temperature using the BSTM device. The original intention was to determine the stress relaxation of the coatings, as explained in section 2.6.3. However, at elevated temperatures unexpected stress-temperature behaviour was observed. The stress in the coatings was not decreasing due to relaxation, but increasing. Fig. 4.13 shows a typical stress-temperature curve as recorded by the BSTM measurements. At temperatures lower than 500 °C, the compressive stress increases due to the different thermal expansion coefficients of coating and substrate. This behaviour is common for coatings with a larger thermal expansion coefficient than the substrate [44]. At a certain temperature though, the curvature is disproportionally increasing, apparently indicating a suddenly rising stress. The bending increases until a measurement is not possible anymore. The laser beams are either not reflected at the upper mirror or do not pass the quartz glass and are reflected only within the vacuum chamber. This huge bending is assumed to be caused by a plastic deformation of the substrate.

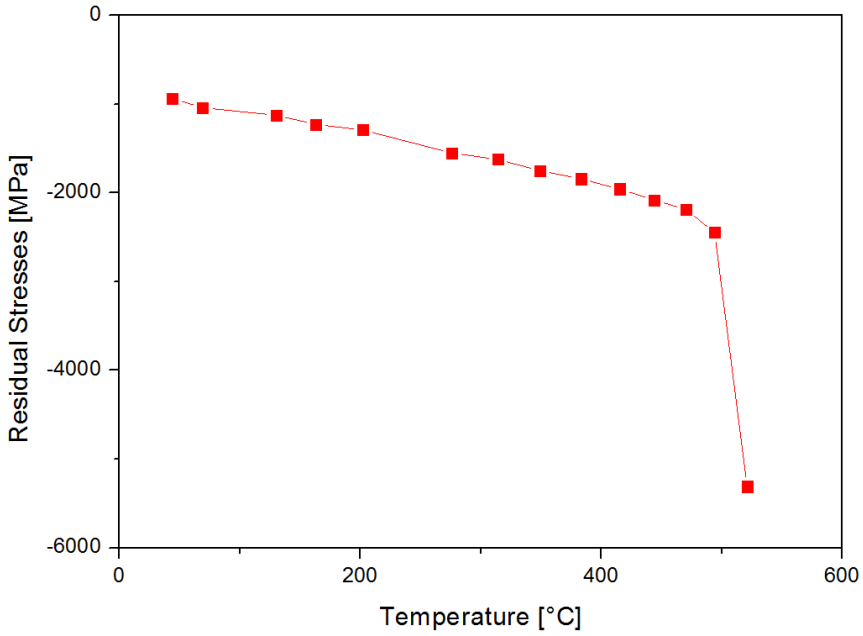

Fig. 4.13: Stress-temperature behaviour of a TiAlN coated silicon substrate, measured using the BSTM device.

To verify the assumption of plastic deformation, further measurements were carried out. Fig. 4.14 displays the results for several sputtered coatings with different bias voltage, deposited on substrates with different thickness. There, the onset temperature for the disproportional deformation depends on the initial residual stress of the coating. The higher

the residual stress is, the earlier deformation occurs during heating. This behaviour is probably as it would be expected for plastic deformation: if the stress in the coating is initially high and additionally increased during heating, the yield strength of the substrate material is reached at lower temperatures. Thus, plastic deformation might also take place at lower temperatures. For the 500 µm thick substrate for instance, which has nearly zero stress at room temperature, the onset temperature of disproportional deformation is 550 °C. The sample with 380 µm substrate thickness has an initial stress level that is significantly higher. Thus, the onset point is lower at approximately 450 °C. No significant difference can be observed in terms of the slope and shape of the curves. No substantial difference between sputtered and arc evaporated coatings was found either, see fig. 4.15.

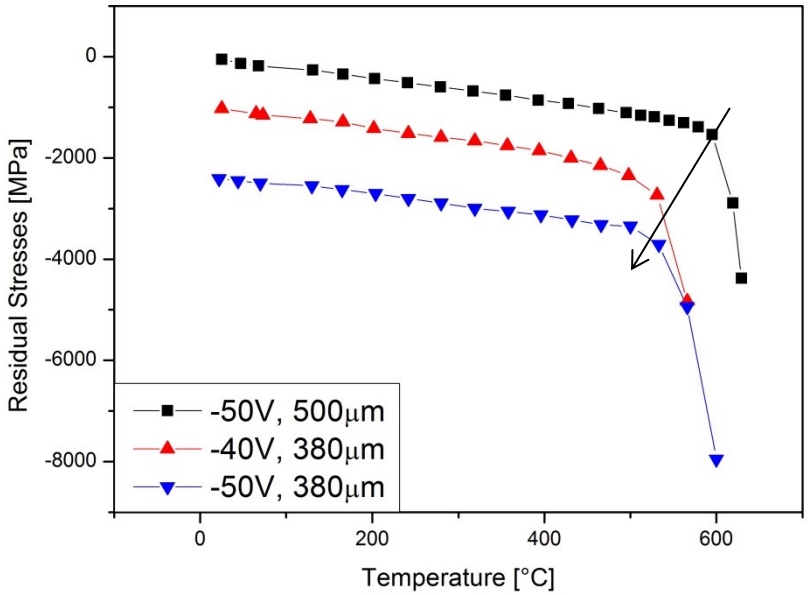

Fig. 4.14: Stress-temperature curves of sputtered TiAlN-coatings with different bias voltage and substrate thickness. The arrow indicates the decrease of the onset point for plastic deformation with higher initial stress.

It needs to be pointed out, that by using the Stoney equation no plasticity is considered. Therefore, the calculated stress values above the onset point for disproportional deformation are not valid.

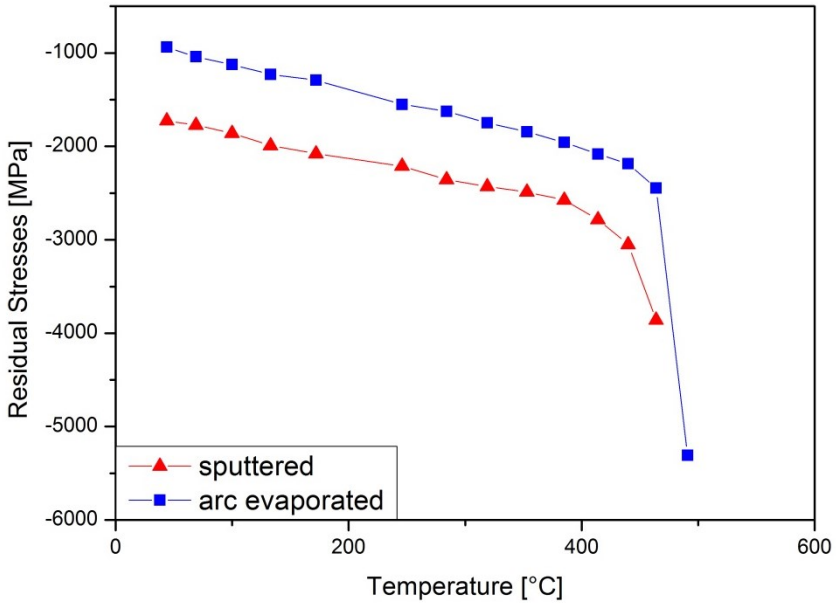

Fig. 4.15: Comparison of a sputtered and an arc evaporated TiAlN-coating.

4.3.2 Isothermal Tests

Throughout the isothermal tests, the substrate curvature is measured as a function of time. The samples are heated up to a defined temperature with maximum heating rate, subsequently the temperature is kept constant. Then, the substrate deformation is measured in defined time intervals. Three sputtered coatings S_50, see table 3.1, were investigated at 400, 430 and 460 °C for more than four hours, see fig. 4.16. The temperatures were chosen with respect to the onset temperature for disproportional deformation, as determined in the non-isothermal tests. The initial stress level was approximately -1500 MPa for all samples.

For the sample measured at 400 °C, the deflection stays constant after the initial heating step, which is typical for mere elastic deformation. On the other hand, at 460 °C a continuous deformation of the sample takes place, although the temperature is constant; this is an indication for creep deformation. Creep strongly depends on diffusion and is thus time and temperature dependent [66]. This results in a steadily ongoing deflection. A situation that is between the two cases can be observed at 430 °C. There, creep deformation starts after certain time and is not as concise as at 460 °C. Therefore, the graphs in fig. 4.16 indicate that there is a transition between mere elastic and creep deformation, at approximately 430 °C.

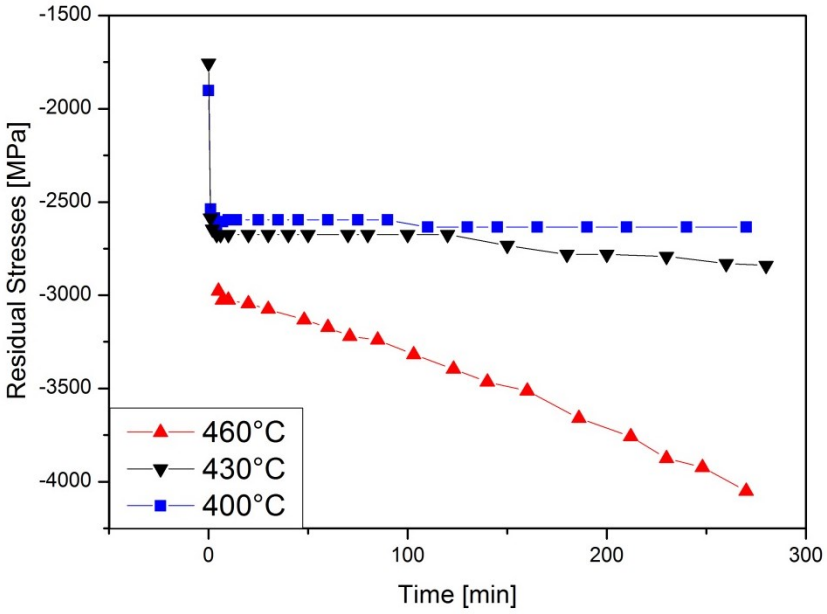

Fig. 4.16: Results of the isothermal tests for sputtered TiAlN at different temperatures. The initial increase in bending is induced by the thermal stress during heating.

4.3.3 Annealing Experiments

Additionally to the isothermal measurements, S_50 samples were annealed in a vacuum furnace of type HTM Reetz. The samples were annealed for 15 minutes at temperatures between 800 °C and 1000 °C in steps of 50 °C. The results are depicted in fig. 4.17 and show, that the observed deformation behaviour is reproducible in other devices as well and is therefore not a specific problem on the BSTM system. It can be seen that the deformation is a function of temperature; it increases proportionally to the annealing temperature.

Fig. 4.17: Samples annealed for 15 min in a vacuum furnace at temperatures from 800 to 1000 °C from left to right, in steps of 50 °C.

According to section 2.5, decomposition of TiAlN into two separate AlN and TiN phases takes place at elevated temperatures, which results in a change of the compressive stresses and hence in deformation of the substrate as well [67]. Therefore, additional samples annealed at 600 and 700 °C were investigated using XRD. The resulting patterns are compared to an as deposited sample, see fig. 4.18. No obvious difference can be noticed between the patterns; the shape of the graph is nearly the same for all three samples. For the coating annealed at

700 °C, an additional peak was measured at 56.2°, which is related to the substrate and has no significance for the coatings. The region between 30 and 36° is depicted in an additional detail in the upper right corner of fig. 4.18. At 33.2° the (100)-peak of hexagonal AlN is located, which is the hexagonal peak with the highest intensity, according to the ICDD database (ICDD 00-025-1133). No peak could be detected in this region for all three patterns. Cubic TiN and cubic AlN could not be detected either. Thus, coating decomposition does not seem to play a role in the observed substrate deformation.

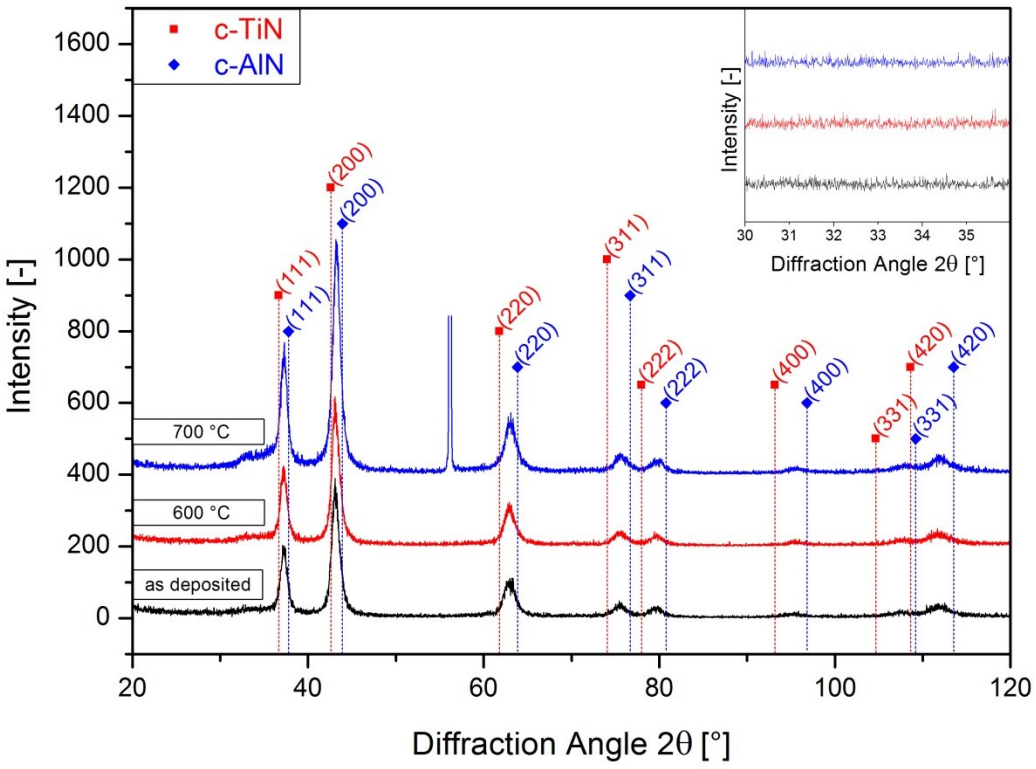

Fig. 4.18: Comparison of the XRD diffractograms of an as deposited S_50 sample and two S_50 samples annealed at 600 and 700 °C for 15 min. The peak positions for cubic TiN and cubic AlN are indicated. In the upper right corner an additional detail of the region between 30 and 36° is depicted.

4.3.4 Stress Distribution in the Samples

In order to verify the assumption of plastic deformation the stresses within the substrate were calculated. The following assumptions were made:

(i) The coating is thin compared to the substrate. Therefore, the stresses within the coatings are assumed to be constant.

(ii) The stress distribution within the substrate is linear [45,68].

These assumptions lead to the stress distribution depicted in fig. 4.19. There, d and t are the coating thickness and the substrate thickness, respectively; σ_c is the compressive stress in the coating determined by the wafer curvature measurements; σ_{max} is the maximum tensile stress in the substrate; s is the distance between the coating and the point of zero stress and w is the width of the sample. The stresses result in corresponding forces that apply in the points indicated in fig. 4.20.

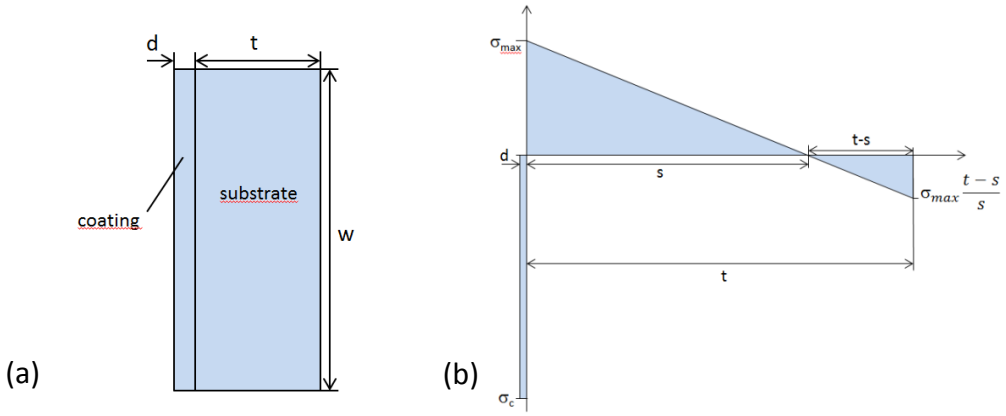

Fig. 4.19: (a) Schematic cross section of the coated sample, (b) stress distribution over the sample thickness. The stress distribution is assumed to be constant in the coating and linear in the substrate.

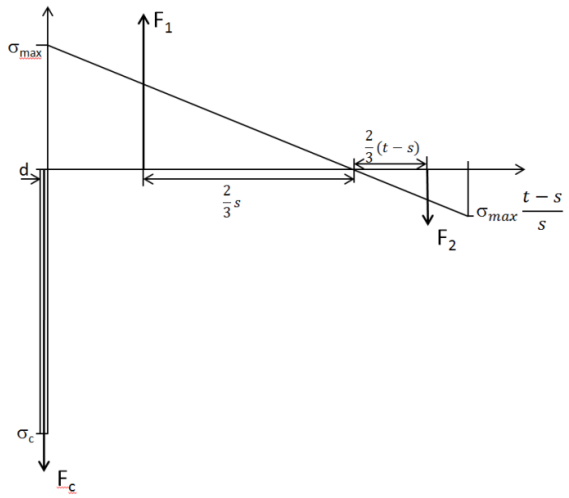

Fig. 4.20: Stress distribution as seen in fig. 4.19 and its corresponding forces.

F_c is the force that stems from the stress in the coating, whereas F_1 and F_2 result from the linear stress distribution in the substrate. Two variables are unknown; σ_{max} and s, which can be determined from the force and momentum equilibrium. In this specific case, the force equilibrium reads:

$$F_1 = F_C + F_2 \tag{4.5}$$

Inserting the forces yields:

$$\frac{1}{2} \cdot \sigma_{max} \cdot s \cdot w = \sigma_c \cdot d \cdot w + \frac{1}{2} \cdot \sigma_{max} \cdot \frac{t-s}{s} \cdot (t-s) \cdot w \tag{4.6}$$

Dividing by w and extracting σ_{max} leads to the following term for σ_{max} :

$$\sigma_{max} = \frac{2 \cdot \sigma_c \cdot d}{s - \frac{(t-s)^2}{s}} \tag{4.7}$$

The momentum equilibrium with respect to the neutral axis reads:

$$F_c \cdot s = \frac{2}{3} \cdot F_1 \cdot s + \frac{2}{3} \cdot F_2 \cdot (t-s) \tag{4.8}$$

Inserting the forces and reducing w yields:

$$\sigma_c \cdot s \cdot d = \frac{1}{3} \cdot \sigma_{max} \cdot s^2 + \frac{1}{3} \cdot \sigma_{max} \cdot \frac{(t-s)^3}{s} \tag{4.9}$$

Introducing eq. (4.7) into (4.9) leads to:

$$3\sigma_c \cdot s \cdot d = \frac{2 \cdot \sigma_c \cdot d}{s - \frac{(t-s)^2}{s}} \cdot s^2 + \frac{2 \cdot \sigma_c \cdot d}{s - \frac{(t-s)^2}{s}} \cdot \frac{(t-s)^3}{s} \tag{4.10}$$

In this equation σ_c and d can be reduced. Therefore, the distance s is neither dependent on the coating stress, nor on the coating thickness. Multiplying eq. (4.10) with the term $s - \frac{(t-s)^2}{s}$ yields:

$$3 \cdot s \cdot \left(s - \frac{(t-s)^2}{s}\right) = 2 \cdot s^2 + \frac{2 \cdot (t-s)^3}{s} \tag{4.11}$$

Expanding the terms, and separating s and t leads to the following, simple relationship:

$$s = \frac{2}{3} \cdot t \tag{4.12}$$

The equation 4.12 corresponds to the calculations carried out by Jansen *et* al. [45]. Inserting eq. (4.12) into (4.7) yields the following equation for the maximum substrate stress:

$$\sigma_{max} = \frac{2 \cdot \sigma_c \cdot d}{\frac{2}{3} \cdot t - \frac{(t - \frac{2}{3} \cdot t)^2}{\frac{2}{3} \cdot t}} = 4 \cdot \sigma_c \cdot \frac{d}{t} \tag{4.13}$$

The maximum stress in the substrate can now be calculated. It has to be pointed out, that due to assumption *(i)* the equation is only valid for substrates that are thick compared to the coating.

It is presumed, that plastic deformation only occurs when the maximum stress in the substrate is higher than the yield strength of the material. Therefore, σ_{max} was calculated at the point of the maximum stress, measured in the BSTM apparatus before disproportional deformation can be detected. This value was subsequently compared to the yield strength of silicon, as reported by Vanderschaeve [69]. Its values for several temperatures and strain rates are given in table 4.8.

Tab. 4.8: Yield strength σ_y for several temperatures T and strain rates $\dot{\varepsilon}$ determined by compression tests [69].

$\dot{\varepsilon}$ = 2 x 10^{-6} s^{-1}		$\dot{\varepsilon}$ = 2 x 10^{-5} s^{-1}		$\dot{\varepsilon}$ = 2 x 10^{-4} s^{-1}	
T [°C]	**σ_y [MPa]**	**T [°C]**	**σ_y [MPa]**	**T [°C]**	**σ_y [MPa]**
300	1900	425	1400	500	1600
350	1700	450	1000	550	1100
400	1100	500	600		
450	600	550	500		
		600	300		

The coating sputtered with -40 V bias, for example, starts to disproportionally deform at a coating stress σ_c of ~ 2500 MPa and at a temperature of approximately 550 °C, see fig. 4.14. For an approximate coating thickness of 5 µm and a substrate thickness of 380 µm, the maximum stress value σ_{max} is roughly 130 MPa. Comparing this value to the yield strength for silicon, at an intermediate strain rate of 2 x 10^{-5} s^{-1} and at 550 °C, shows that there is a

recognisable difference of 370 MPa. This result would suggest that plastic deformation might not be the reason for the disproportional deflection of the silicon samples. However, it needs to be mentioned that the deformation of the substrates depends on the substrate orientation and stress distribution. Therefore, they might deform differently to the compressive load behaviour reported by Vanderschaeve [69].

5 Summary and Conclusions

Three major subjects were treated within this work to optimize a device for characterisation of the stress-temperature dependence of TiAlN based coatings:

(i) a new heating system was installed and calibrated,

(ii) the investigated coatings were analysed with respect to composition, microstructure, mechanical properties and thermal expansion coefficient

(iii) unusual stress-temperature behaviour was interpreted by plastic deformation of the substrate material.

Ad (i): In order to obtain a homogenous temperature distribution, a new heating system, consisting of a silicon nitride heating plate, with two separate 2000 W heating circles, was installed. To support the heating plate, a new mounting system was constructed as well. To control the temperature of the heating plate, a multichannel controller was used. The controller was calibrated with respect to settling time, heating rate, cooling rate and temperature overshoot. The homogenous temperature distribution of the heating plate was examined and confirmed by thermographic measurements. A temperature difference between the investigated substrates and the heating plate was observed due to a low heat transfer between both. Therefore, it could not be assumed that the temperature of the substrate is the same as set on the controller. Thus, an additional thermocouple was installed on a supplementary silicon strip on the heating plate. The temperature given from the thermocouple was compared to the melting point of pure indium, tin and lead. A constant difference of approximately 30 °C was observed. By correcting the measured temperatures with this value, the accuracy was enhanced to ± 10 °C. It was also found that the temperature difference can be reduced by 50 °C, by performing the measurements at ambient pressure. However, oxidation of the electric contacts might be a problem at high temperatures. Hence, no yield in absolute temperature could be achieved.

Ad (ii): The coatings were compared with respect to composition, microstructure, hardness and Young´s modulus. Moreover, the thermal expansion coefficient was calculated. It was found that compared to the target composition, the tantalum content was increased during deposition. The aluminium content on the other hand was slightly decreased. The microstructure of the coatings was face centred cubic for the sputtered and for the arc evaporated coatings with a Ti/Al ratio of 50/50. The arc evaporated coatings with a Ti/Al ratio of 33/67 had a microstructure consisting of cubic and hexagonal parts. Hardness and Young´s modulus were both lower for the coatings with a hexagonal fraction. The bias voltage showed no substantial influence on the mechanical properties. It was also found that incorporation of tantalum raises the residual compressive stresses at room temperature. The

value of the thermal expansion coefficient of the coatings with a hexagonal fraction was closer to the value of hexagonal AlN, compared to the other coatings. No influence of the bias voltage could be observed on the thermal expansion coefficient.

Ad (iii): A disproportional deflection of coated silicon samples was observed during non-isothermal BSTM measurements. This effect was assumed to be caused by plastic substrate deformation. It was found that the onset temperature for this effect is dependent on the initial stress level of the coating. The higher the stress level is, the lower is the onset temperature. Isothermal measurements were additionally carried out, where this effect could also be detected. At temperatures higher than 430 °C, the substrate deforms continuously although the temperature is kept constant, which might be an indication for creep. The disproportional substrate bending was also observed for samples annealed in vacuum at temperatures between 800 and 1000 °C. No decomposition, which could explain the disproportional deformation, was found. A mathematic equation for the maximum stress in the substrate was derived from a force and momentum equilibrium. The obtained maximum stress was compared to the yield stress of silicon. The calculated stress did not exceed the yield strength of Si, which would be an evidence for plastic deformation. However, the silicon substrates are single crystalline and might therefore behave differently, than assumed in the calculations.

In conclusion, a reliable heating system with a homogenous temperature distribution was installed and calibrated. The temperature accuracy and the measurement time were significantly enhanced, allowing several samples to be measured at the same time under comparable conditions. Also, a simple equation for calculating the maximum stress in the substrates was derived. Comparing this value to the yield strength of silicon did not provide a sufficient explanation for the observed deformation. However, as the used substrates are (100) oriented single crystals, they might have a different deformation behaviour than assumed in the calculations. Therefore, further investigation would be of interest with respect to the plastic deformation behaviour of coated single crystals. Varying the orientation or using a different substrate material, might result in adequate measurements and would be of interest for future work.

References

[1] S.G. Harris, E.D. Doyle, A.C. Vlasveld, P.J. Dolder, Dry cutting performance of partially filtered arc deposited titanium aluminium nitride coatings with various metal nitride base coatings, Surf. Coat. Technol. 146–147, 305-311, 2001.

[2] G.S. Fox-Rabinovich, G.C. Weatherly, A.I. Dodonov, A.I. Kovalev, L.S. Shuster, S.C. Veldhuis, G.K. Dosbaeva, D.L. Wainstein, M.S. Migranov, Nano-crystalline filtered arc deposited (FAD) TiAlN PVD coatings for high-speed machining applications, Surf. Coat. Technol. 177–178, 800-811, 2004.

[3] A. Buranawong, N. Witit-anun, S. Chaiyakun, A. Pokaipisit, P. Limsuwan, The effect of titanium current on structure and hardness of aluminium titanium nitride deposited by reactive unbalanced magnetron co-sputtering, Thin Solid Films 519 (15), 4963-4968, 2011.

[4] D. McIntyre, J.E. Greene, G. Håkansson, J.E. Sundgren, W.D. Münz, Oxidation of metastable single-phase polycrystalline $Ti_{0.5}Al_{0.5}N$ films: Kinetics and mechanisms, J. Appl. Phys. 67 (3), 1542-1553, 1989.

[5] R. Daniel, K.J. Martinschitz, J. Keckes, C. Mitterer, The origin of stresses in magnetron-sputtered thin films with zone T structures, Acta Mater. 58, 2621-2633, 2010.

[6] M. Ahlgren, H. Blomqvist, Influence of bias variation on residual stress and texture in TiAlN PVD coatings, Surf. Coat. Technol. 200 (1–4), 157-160, 2005.

[7] Guo-an Cheng, Dong-yan Han, Chang-lin Liang, Xiao-ling Wu, Rui-ting Zheng, Influence of residual stress on mechanical properties of TiAlN thin films, Surf. Coat. Technol. 228 (1), 328-330, 2013.

[8] B. Breidenstein, B. Denkena, Significance of residual stress in PVD-coated carbide cutting tools, CIRP Annals - Manufacturing Technology 62 (1), 67-70, 2013.

[9] K.J. Martinschitz, R. Daniel, C. Mitterer, J. Keckes, Stress evolution in CrN/Cr coating systems during thermal straining, Thin Solid Films 516, 1972-1976, 2007.

[10] C.A. Sciammarella, A. Boccaccio, L. Lamberti, C. Pappalettere, A. Rizzo, M.A. Signore, D. Valerini, Measurements of deflection and residual stress in thin films: Utilizing coherent light reflection/projection, Moiré interferometry, Exp. Mech. 53, 977-987, 2013.

[11] D. Petersohn, H. Sander, PVD-Verschleißschutzschichten, Dünnschichttechnik, 993-1000, 1996.

[12] Fr.-W. Bach, T. Duda, Moderne Beschichtungsverfahren, Wiley-VCH, Weinheim, 2000.

[13] R.A. Haefer, Oberflächen- und Dünnschichttechnologie, Teil I: Beschichtungen von Oberflächen, Springer, Berlin, Heidelberg, 1987.

[14] F. Löffler, A. Barimani, PVD-Schichten für den tribologischen Einsatz, Ingenieur Werkstoffe 2, Springer-VDI, Düsseldorf, 56-59, 1990.

[15] H. Frey, Vakuumbeschichtung 1, Plasmaphysik- Plasmadiagnostik- Analytik, VDI, Düsseldorf, 1995.

[16] B. Rother, J. Vetter, Plasmabeschichtungsverfahren und Hartstoffschichten, Deutscher Verlag für Grundstoffindustrie, Leipzig, 1992.

[17] W.D. Westwood, Sputter Deposition, AVS, New York, 2003.

[18] W.D. Sproul, High-rate reactive DC magnetron sputtering of oxide and nitride superlattice coatings, Vacuum 51, 641-646, 1998.

[19] Aultimut international L.L.C., Technologies, plasma technologies, www.aultimut.com, January 2014.

[20] G. Kienel, Vakuumbeschichtung 4, Anwendungen Teil 1, VDI, Düsseldorf, 1993.

[21] S. Grasser, R. Daniel, C. Mitterer, Microstructure modifications of CrN coatings by pulsed bias sputtering, Surf. Coat. Technol. 206, 4666-4671, 2012.

[22] G. Greczynski, J. Lu, J. Jensen, I. Petrov, J.E. Greene, S. Bolz, W. Kölker, Ch. Schiffers, O. Lemmer, L. Hultman, Strain-free, single-phase metastable $Ti_{0.38}Al_{0.62}N$ alloys with high hardness: Metal-ion energy vs. momentum effects during film growth by hybrid high-power pulsed/dc magnetron cosputtering, accepted, doi:10.1016/j.tsf.2014.01.017, 2014.

[23] N. Schalk, C. Mitterer, J. Keckes, M. Penoy, C. Michotte, Influence of residual stresses and grain size on the spinodal decomposition of metastable $Ti_{1-x}Al_xN$ coatings, Surf. Coat. Technol. 209, 190-196, 2012.

[24] M. Ohring, The Materials Science of Thin Films – Deposition and Structure, Academic Press, San Diego, Second edition, 2002.

[25] R.D. Arnell, P.J. Kelly, Recent advances in magnetron sputtering, Surf. Coat. Technol. 112, 170-176, 1999.

[26] L. Combadiere, J. Machet, Study and control of both target-poisoning mechanisms and reactive phenomenon in reactive planar magnetron cathodic sputtering of TiN, Surf. Coat. Technol. 82, 145-157, 1996.

[27] D. M. Mattox, Vacuum Deposition Processes, www.pfonline.com/articles/069901.html, January 2014.

[28] H.K. Pulker, Arc evaporation – An overview, Vakuum in Forschung und Praxis 11 (1), 25, 1999.

[29] D.M. Sanders, A. Anders, Review of cathodic arc deposition technology at the start of the new millennium, Surf. Coat. Technol. 133-134, 78-90, 2000.

[30] U. Helmersson, M. Lattemann, J. Bohlmark, A.P. Ehiasarian, J.T. Gudmundsson, Ionized physical vapor deposition (IPVD): A review of technology and applications, Thin Solid Films 513 (1-2), 1-24, 2006.

[31] R.L. Boxman, S. Goldsmith, Macroparticle contamination in cathodic arc coatings: generation, transport and control, Surf. Coat. Technol. 52, 39-50, 1992.

[32] A. Hörling, L. Hultman, M. Odén, J. Sjölén, L. Karlsson, Thermal stability of arc evaporated high aluminum content $Ti_{1-x}Al_xN$ thin films, J. Vac. Sci. Technol. A 20 (5), 1815-1923, 2002.

[33] H. Lüth, Solid Surfaces, Interfaces and Thin Films, Springer, Berlin - Heidelberg - New York, 2001.

[34] S. Mukherjee, D. Gall, Structure zone model for extreme shadowing conditions, Thin Solid Films 527, 158-163, 2013.

[35] P.B. Barna, M. Adamik, Fundamental structure forming phenomena of polycrystalline films and the structure zone models, Thin Solid Films 317 (1-2), 27 -33, 1998.

[36] B.A. Movchan, A.V. Demchishin, Study of the structure and properties of thick vacuum condensates of nickel, titanium, tungsten, aluminium oxide and zirconium dioxide, Phy. Met. Metallogr. 28, 653-660, 1969.

[37] J.A. Thornton, Influence of apparatus geometry and deposition conditions on the structure and topography of thick sputtered coatings, J. Vac. Sci. Technol. 11 (4), 666-670, 1974.

[38] R. Messier, A.P. Giri, R.A. Roy, Revised structure zone model for thin film physical structure, J. Vac. Sci. Technol. A 2 (2), 500-503, 1984.

[39] S. PalDey, S.C. Deevi, Single layer and multilayer wear resistant coatings of (Ti,Al)N: a review, Mater. Sci. Eng. 342 , 58-79, 2003.

[40] Li Chen, Yong Du, Fei Yin, Jia Li, Mechanical properties of (Ti, Al)N monolayer and TiN/(Ti, Al)N multilayer coatings, Int. J. Refract. Met. H 25 (1), 72-76, 2007.

[41] M. Pfeiler, G.A. Fontalvo, J. Wagner, K. Kutschej, M. Penoy, C. Michotte, C. Mitterer, M. Kathrein, Arc evaporation of Ti-Al-Ta-N Coatings: The effect of bias voltage and Ta on high-temperature tribological properties, Tribol. Lett. 30, 91-97, 2008.

[42] Y. Yin, D. McKenzie, M. Bilek, Intrinsic stress induced by substrate bias in amorphous hydrogenated silicon thin films, Surf. Coat. Technol. 198 (1-3), 156-160, 2005.

[43] T.W. Clyne, in P.J. Withers (ed), “Residual Stresses in Thick and Thin Surface Coatings”, Encyclopedia of Materials: Science and Technology, Elsevier, Amsterdam, 2001.

[44] R. Daniel, D. Holec, M. Bartiosik, J. Keckes, C. Mitterer, Size effect of thermal expansion and thermal/intrinsic stresses in nanostructured thin films: Experiment and model, Acta Mat. 59 (17), 6631-6645, 2011.

[45] G.C.A.M. Janssen, M.M. Abdalla, F. van Keulen, B.R. Pujada, B. van Venrooy, Celebrating the 100th anniversary of the Stoney equation for film stress: Developments from polycrystalline steel strips to single crystal silicon wafers, Thin Solid Films 517, 1858-1867, 2009.

[46] G. Kienel, Vakuumbeschichtung 3, Anlagenautomatisierung – Meß- und Analysentechnik, VDI, Düsseldorf, 1994.

[47] A.C. Fischer-Cripps, Critical review of analysis and interpretation of nanoindentation test data, Surf. Coat. Technol. 200 (14-15), 4153-4165, 2006.

[48] Rocky Mountain Instrument Co., Technical Note/Transmission Curves, www.rmico.com, January 2014.

[49] Korth Kristalle GmbH, Material/Bariumfluorid, www.korth.de, January 2014.

[50] D. Winkler, Konzeption und Realisierung eines thermisch unterstützten Meßverfahrens zur Bestimmung von Eigenspannungen in dünnen Schichten, Diploma Thesis, Montanuniversität Leoben, 1997.

[51] P.H. Mayrhofer, Materials science aspects of nanocrystalline PVD hard coatings, PhD Thesis, Montanuniversität Leoben, 2001.

[52] F. Christian, T. Narita, Siliconizing of molybdenum metal in indium-silicon melts, Mater. T. JIM 39 (6), 658-662, 1998.

[53] R.W. Olesinski, G.J. Abbaschian, The Si-Sn (silicon-tin) system, Bull. Alloy Phase Diagr. 5 (3), 273-276, 1984.

[54] R.W. Olesinski, G.J. Abbaschian, The Pb-Si (lead-silicon) system, Bull. Alloy Phase Diagr. 5 (3), 271-273, 1984.

[55] R. B. Ross, Metallic Materials, Chapman and Hall Ltd., London, 1968.

[56] JUMO GmbH & Co KG, Products/Temperature/Controllers (electronic)/multichannel controllers/JUMO 500/ Documentation, www.jumo.de, January 2014.

[57] R.M. Spriggs, S.L. Bender, Vegard´s law and the System alumina-chromia, J. Am. Ceram. Soc. 45 (10), 506,

[58] K. Kutschej, P.H. Mayrhofer, M. Kathrein, P. Polcik, R. Tessadri, C. Mitterer, Structure, mechanical and tribological properties of sputtered $Ti_{1-x}Al_xN$ coatings with $0.5 \leq x \leq 0.75$, Surf. Coat. Technol. 200 (7), 2358-2365, 2005.

[59] K. Kutschej, P.H. Mayrhofer, M. Kathrein, C. Michotte, P. Polcik, C. Mitterer, Multi-functional multi-component $Ti_{1-x}Al_xN$ based Coatings, Proceedings of the 16th International Plansee Seminar 2005, 774–788, Plansee Holding AG, Reutte, Austria, 2005.

[60] M. Pfeiler, K. Kutschej, M. Penoy, C. Michotte, C. Mitterer, M. Kathrein, The influence of bias voltage on structure and mechanical/tribological properties of arc evaporated Ti-Al-V-N coatings, Surf. Coat. Technol. 202, 1050-1054, 2007.

[61] K. Chu, P.W. Shum, Y.G. Shen, Substrate bias effects on mechanical and tribological properties of substitutional solid solution (Ti, Al)N films prepared by reactive magnetron sputtering, Mat. Sci. Eng. B 131, 62-71, 2006.

[62] D.B. Lewis, L.A. Donohue, M. Lembke, W.-D. Münz, R. Kunzel Jr., V. Valvoda, C.J. Blomfield, The influence of the yttrium content on the structure and properties of $Ti_{1-x-y-z}Al_xCr_yY_zN$ PVD hard coatings, Surf. Coat. Technol. 114, 187-199, 1999.

[63] H.-Y. Chen, J.-H. Chen, F.-H. Lu, Evaluation of Poisson´s ratio and Young´s modulus of nitride films by combining grazing incidence X-ray diffraction and laser curvature techniques, Thin Solid Films 516, 345-348, 2007.

[64] Accuratus Corporation, Materials/Aluminium Nitride, www.acuratus.com, February 2014.

[65] BryCoat Inc., coating services/PVD coatings/titanium nitride TiN/TiN physical properties, www.brycoat.com, February 2014.

[66] T.H. Courtney, Mechanical Behaviour of Materials, McGraw-Hill, Boston, 2000.

[67] M. Bartosik, R. Daniel, Z. Zhang, M. Deluca, W. Ecker, M. Stefenelli, M. Klaus, C. Genzel, C. Mitterer, J. Keckes, Lateral gradients of phases, residual stress and hardness in a laser heated $Ti_{0.52}Al_{0.48}N$ coating on hard metal, Surf. Coat. Technol. 206, 4502-4510, 2012.

[68] A. Brenner, S. Senderoff, Calculation of stress in electrodeposits from the curvature of a plated strip, J. Res. Nat. Bur. Stand. 42, 105-123, 1949.

[69] G. Vanderschaeve, in: R. Hull (ed.), “Mechanical behaviour of Si at low temperature”, Properties of Crystalline Silicon, The Institution of Electrical Engineers, London, 136-142, 1999.